Clim Dyn
DOI 10.1007/s00382-013-1968-5

Mean meridional currents in the central and eastern equatorial Atlantic

Renellys C. Perez · Verena Hormann · Rick Lumpkin · Peter Brandt · William E. Johns · Fabrice Hernandez · Claudia Schmid · Bernard Bourlès

Received: 4 June 2013 / Accepted: 8 October 2013

Abstract Ship-based acoustic Doppler current profiler (ADCP) velocity measurements collected by several major field programs in the tropical Atlantic are averaged and combined with estimates of the mean near-surface velocity derived from drifters and Argo float surface drifts (ADCP+D) to describe the mean cross-equatorial and vertical structure of the meridional currents along 23°W and 10°W. Data from moored ADCPs and fixed-depth current meters, a satellite-derived velocity product, and a global ocean reanalysis were additionally used to evaluate the mean ADCP+D meridional velocity. The dominant circulation features in the long-term mean ADCP+D meridional velocity in the upper 100 m are the tropical cells (TCs) located approximately between 5°S and 5°N, with near-surface poleward flow and subsurface equatorward flow that is stronger and shallower in the northern cell compared to the southern cell. The thickness of the surface limb of the TCs decreases and the northern cell is found to shift further south of the equator from the central to eastern tropical Atlantic. Analysis of two-season means estimated from the ship-based ADCP, near-surface drift, and moored velocity data, as well as the simulated fields, indicates that the maximum poleward velocity in the surface limb of the TCs intensifies during December–May along 23°W largely due to seasonal compensation between the geostrophic and ageostrophic (or wind-driven) components of the meridional velocity, whereas the maximum equatorward flow in the subsurface limb of the northern cell intensifies during June–November along both 23°W and 10°W due to the seasonality of the geostrophic meridional velocity.

This paper is a contribution to the special issue on tropical Atlantic variability and coupled model climate biases that have been the focus of the recently completed Tropical Atlantic Climate Experiment (TACE), an international CLIVAR program (http://www.clivar.org/organization/atlantic/tace). This special issue is coordinated by William Johns, Peter Brandt, and Ping Chang, representatives of the TACE Observations and TACE Modeling and Synthesis working groups.

R. C. Perez
Cooperative Institute for Marine and Atmospheric Studies, University of Miami, 4600 Rickenbacker Causeway, Miami, FL 33149, USA

R. C. Perez (✉) · R. Lumpkin · C. Schmid
NOAA Atlantic Oceanographic and Meteorological Laboratory, Miami, FL, USA
e-mail: Renellys.C.Perez@noaa.gov

V. Hormann
Scripps Institution of Oceanography, University of California, San Diego, La Jolla, CA, USA

P. Brandt
GEOMAR Helmholtz-Zentrum für Ozeanforschung Kiel, Kiel, Germany

W. E. Johns
Rosenstiel School of Marine and Atmospheric Science, University of Miami, Miami, FL, USA

F. Hernandez
Institut de Recherche pour le Développement, Mercator-Océan, Toulouse, France

B. Bourlès
Institut de Recherche pour le Développement, LEGOS, Brest, France

Published online: 31 October 2013

Keywords Tropical Atlantic · Meridional currents · Tropical cells

1 Introduction

Since the late 1990s, several major field programs have been initiated to monitor the circulation, hydrography, and air-sea fluxes in the central and eastern equatorial Atlantic with moored arrays (e.g., Bourlès et al. 2008). Concurrent with these field programs, a large number of cross-equatorial cruises have been conducted primarily along 23°W and 10°W to survey zonal and meridional currents with shipboard and lowered acoustic Doppler current profilers (ADCPs) as well as temperature, salinity, and dissolved oxygen (Fig. 1). These cruises were also used to opportunistically deploy satellite-tracked drifting buoys (hereafter "drifters") and Argo floats. With these measurements, as well as data collected by earlier programs such as the Seasonal Response of the Equatorial Atlantic (SEQUAL) and Programme Française Océan-Climat en Atlantique Equatorial (FOCAL) programs, much has been learned about the mean cross-equatorial structure and seasonal-to-interannual variability of zonal currents, temperature, salinity, and dissolved oxygen in the upper water column in the central and eastern equatorial Atlantic (e.g., Garzoli 1987; Grodsky et al. 2005; Brandt et al. 2006, 2008, 2010; Hormann and Brandt 2007, 2009; Bunge et al. 2007; Kolodziejczyk et al. 2009; Hummels et al. 2013), but the meridional currents have yet to be examined.

Based on previous analytical and numerical modeling studies (e.g., McCreary and Lu 1994; Liu et al. 1994; Malanotte-Rizzoli et al. 2000; Hazeleger et al. 2003; Schott et al. 2004; Lohmann and Latif 2007) and observations collected in the tropical Atlantic between 40°W and 30°W (e.g., Molinari et al. 2003), it is expected that the mean cross-equatorial structure of the meridional currents along 23°W and 10°W will be governed by shallow overturning circulation cells known as tropical cells (TCs) which appear as near-surface, near-equatorial maxima of the much larger subtropical cells. The TCs are confined to the upper 100 m of the water column, and are characterized by wind-driven equatorial upwelling, poleward wind-driven flow in the surface limb, off-equatorial downwelling at about ±3–5° latitude, and equatorward geostrophic flow in the subsurface limb. However, this simple depiction of the flow is complicated by the presence of strong fronts bounding the seasonal equatorial Atlantic cold tongue which exhibit large undulations (Fig. 1a) due to tropical instability waves (TIWs; e.g., Düing et al. 1975; Legeckis

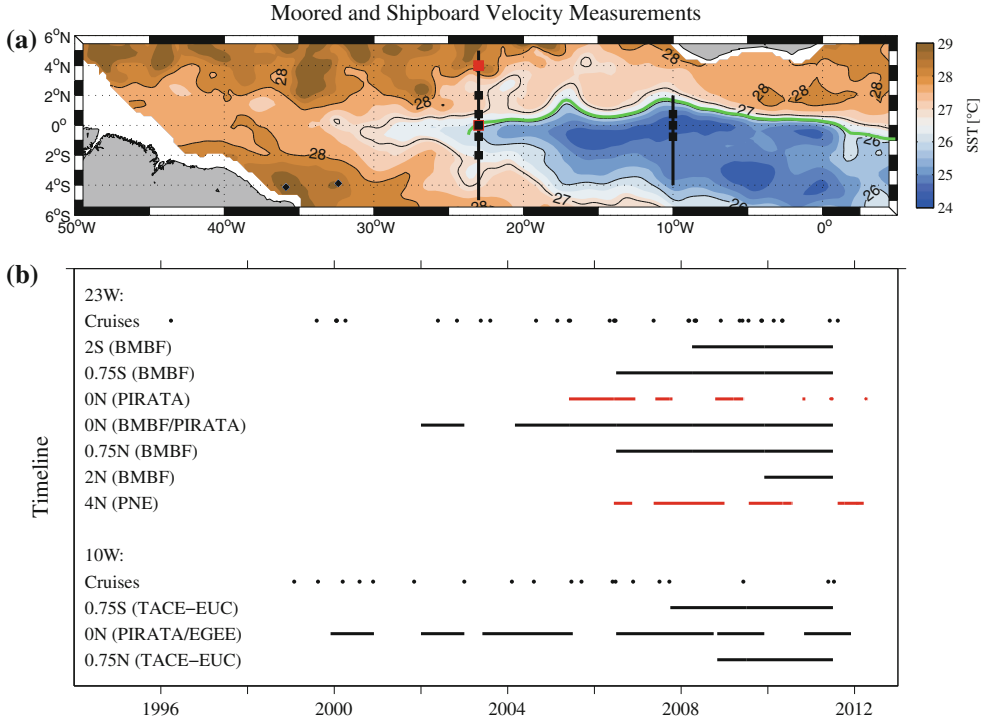

Fig. 1 **a** Map and **b** timeline of moored and shipboard observations used in this study. *Red* (*black*) *squares* in (**a**) indicate locations of fixed-depth current meter moorings (moored ADCPs), and *black vertical lines* mark the most-frequently sampled latitudinal range of the shipboard sections. *Color shading* in (**a**) is TMI SST on the 21-June-2006 onset of the equatorial Atlantic cold tongue, with the position of the northern front identified by the median frontal SST methodology of Hormann et al. (2013) overlaid as a *green line*. *Red* (*black*) *horizontal lines* in (**b**) indicate the approximate current meter (moored ADCP) time periods, *black dots* mark individual ship cruises

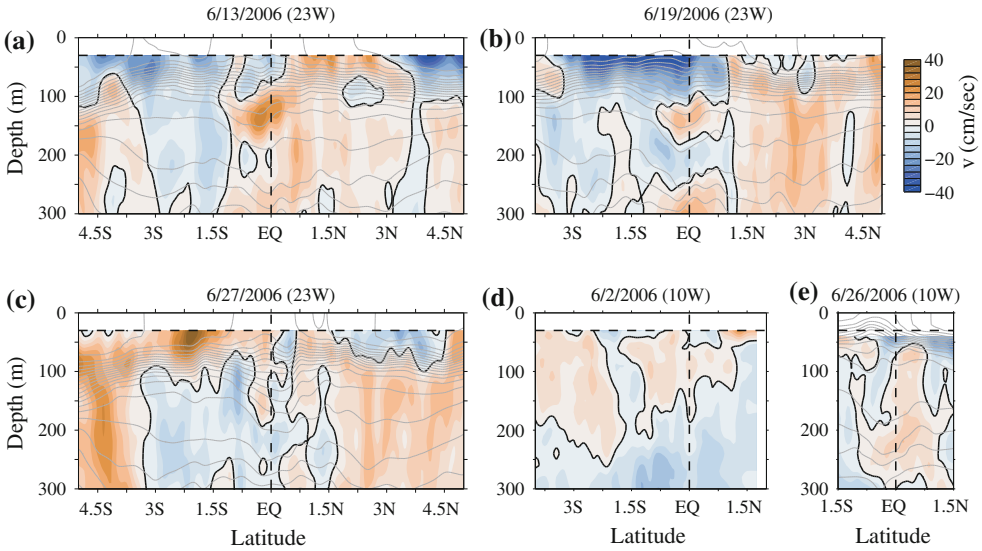

Fig. 2 Distribution of ship-based ADCP meridional velocity sampled in June 2006 (date refers to equatorial crossing) along **a**–**c** 23°W and **d**, **e** 10°W in cm s^{-1}. *Black contour* indicates the 0 cm s^{-1} velocity contour. When available, corresponding temperatures are contoured in *gray* in 1 °C increments

and Reverdin 1987; Steger and Carton 1991; Hormann et al. 2013). The cold tongue and TIWs are typically most pronounced in boreal summer associated with increased southeasterly trade winds and enhancement of the shear between the equatorial zonal currents (e.g., Legeckis and Reverdin 1987; Steger and Carton 1991; Grodsky et al. 2005; Brandt et al. 2011a; Perez et al. 2012; Hormann et al. 2013). During this time of year, large meridional velocity fluctuations associated with TIWs can be seen in shipboard sections collected along 23°W and 10°W. For instance, the poleward flow observed between 30 and 100 m depth along 23°W a few days before (Fig. 2b) the cold tongue onset on June 21, 2006 (Brandt et al. 2011a; Hormann et al. 2013) changes to equatorward flow 1 week later (Fig. 2c). Because the equatorial Atlantic circulation from the surface down to the thermocline is so profoundly influenced by westward propagating TIWs and other mesoscale phenomena (e.g., Düing et al. 1975; Weisberg and Weingartner 1988; Menkes et al. 2002; Foltz et al. 2004; Grodsky et al. 2005; Bunge et al. 2007; Dutrieux et al. 2008; von Schuckmann et al. 2008; Jouanno et al. 2013), to date in situ current measurements have been insufficient to estimate the much smaller (on the order of 10 cm s^{-1}) mean meridional currents or their seasonal variations.

Without representations of the mean cross-equatorial structure and seasonal variability of the meridional velocity derived from shipboard and moored observations, the realism of simulated meridional currents produced by ocean general circulation models (OGCMs), assimilation models, and coupled climate models (e.g., Hazeleger et al. 2003; Lohmann and Latif 2007; Athié et al. 2009; Giordani and Caniaux 2011; Richter et al. 2013) cannot be assessed in the same fashion as simulated zonal currents (e.g., Hormann and Brandt 2007; Seo et al. 2007; Rabe et al. 2008; Giordani and Caniaux 2011; Seo and Xie 2011). An improved characterization of the upper-ocean meridional currents is needed because numerical models such as those above are being used to understand the two distinct patterns of coupled ocean–atmosphere variability dominating climate fluctuations in the tropical Atlantic region on interannual to decadal time scales: the thermodynamic meridional mode and the dynamic zonal mode or Atlantic Niño mode (e.g., Chang et al. 2006, and references therein; Richter et al. 2013; Lübbecke 2013). Recent studies suggest that meridional currents play an important role in Atlantic meridional mode dynamics by advecting wind-driven warm temperature anomalies induced immediately north of the equator towards the equatorial region and leading to so-called non-canonical Atlantic Niño events in boreal summer and fall (Richter et al. 2013; Lübbecke 2013). During these non-canonical Atlantic Niño events, equatorial warming by meridional advection was found to be most pronounced in boreal summer between 20 and 40 m depth (Richter et al. 2013). Meridional currents may similarly contribute to anomalous cooling events in the tropical Atlantic, such as the strong cooling observed in the ATL3 region (i.e., 20°W–0°, 3°S–3°N) from May to July 2009 (Foltz et al. 2012; Brandt et al. 2013) by advecting subsurface cold temperature anomalies induced in the northern hemisphere.

In this study, measurements collected primarily along 23°W and 10°W during the past two decades are used for the first time to describe: (1) the long-term mean cross-equatorial and vertical structure of the meridional currents in the central and eastern equatorial Atlantic, and (2) the seasonal means during the months December to May (hereafter Dec–May) when the Atlantic cold tongue is absent or weak and June to November (hereafter Jun–Nov) when the cold tongue is most pronounced and meridional velocity may play a role in the development of non-canonical Atlantic Niño events. The paper outline is as

follows: The data sets, global ocean reanalysis, and the methods applied to process and combine the data sets are described in Sect. 2. The structure of the long-term meridional velocity obtained from the observations and the reanalysis product, as well as the differences between the structure of the Dec–May and Jun–Nov mean meridional velocities, are examined in Sect. 3. Finally in Sect. 4, the results are summarized and discussed in the context of previous tropical Atlantic studies.

2 Data sets, reanalysis products, and methods

2.1 Shipboard data

Shipboard data were obtained during March 1996 to August 2011 from 36 latitude-depth transects in the central (between 22°W and 29°W, nominally 23°W) and 19 transects in the eastern (10°W) equatorial Atlantic (Fig. 1b). Most of these sections are presented in Brandt et al. (2006, 2010) and Kolodziejczyk et al. (2009), and additional sections are available from recent Prediction and Research Moored Array in the Tropical Atlantic (PIRATA) Northeast Extension (PNE; cf. Hormann et al. 2013) and Tropical Atlantic Circulation Experiment—Equatorial Undercurrent (TACE-EUC; cf. Subramaniam et al. 2013) cruises. The individual transects resolve the flow from the near surface (typically 30 m) down to some intermediate depth (250 m or deeper). Uncertainties of hourly shipboard ADCP (SADCP) averages were estimated to be better than 2–4 cm s^{-1} (Fischer et al. 2003) while the accuracy of lowered ADCP (LADCP) data was assumed to be better than 5 cm s^{-1} (Visbeck 2002). Despite the larger LADCP uncertainty, we retain these data as calibrated SADCP measurements were not available for three January sections along 23°W which represent the only realizations for this month. When both LADCP and SADCP measurements are available, the current data are merged with respect to the higher accuracy and better horizontal resolution of the SADCP measurements—SADCP measurements are weighted up to five times more strongly than LADCP measurements. The merged data are mapped onto a uniform 0.05° latitude by 10 m depth grid using a Gaussian interpolation scheme with horizontal and vertical cutoff radii of twice the grid resolution (see Brandt et al. 2010 for details). Calibrated hydrographic parameters (temperature, salinity, and dissolved oxygen) are not available for all of the cruises along 23°W and 10°W. Hence, the ship-based ADCP measurements were merged and averaged in depth coordinates rather than isopycnal coordinates (e.g., Johnson et al. 2002).

Although shipboard sections have been collected during all four seasons, there are seasonal sampling biases with the majority of samples collected during boreal spring along 23°W and during boreal summer along 10°W (Fig. 3).

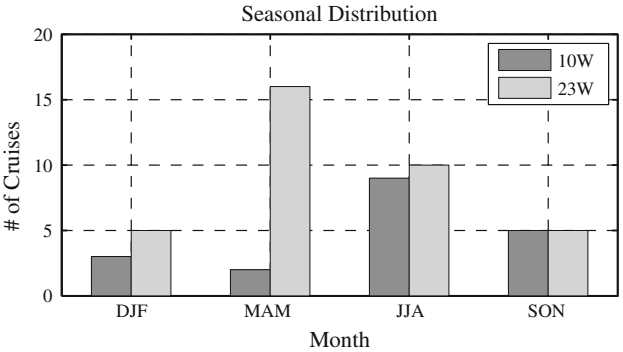

Fig. 3 Seasonal distribution of the ship-based ADCP sections along 23°W (*light gray*) and 10°W (*dark gray*)

Despite these seasonal biases, the samples along 23°W are distributed in such a way that they can be partitioned fairly evenly into boreal winter and spring (21 samples during Dec–May) as well as boreal summer and fall (15 samples during Jun–Nov). There are too few samples to perform a similar meaningful seasonal breakdown along 10°W (Fig. 3). With the exception of June 2006 when multiple sections were collected in 1 month (Fig. 2), individual cruises typically occur several months apart from one another, and we assume that each section represents an independent sample. The presence of TIWs, which have periodicities of 14–50 days and O (1,000 km) zonal wavelengths (e.g., Legeckis 1977; Qiao and Weisberg 1995; Athié and Marin 2008), allows us to assume that the meridional velocity sections collected in June 2006 are also independent of one another.

2.2 Drifter and Argo data

As the currents above 30 m are not well resolved by the ship-based ADCP instruments, 6-hourly velocity measurements obtained from satellite-tracked drifters collected in the region bounded by 30°W–8°W, 20°S–20°N and spanning the period July 9, 1992 to June 30, 2012, as well as near-surface velocities constructed from Argo float surface trajectories from July 29, 1997 to May 7, 2013 from the YoMaHa'07 data set (Lebedev et al. 2007), are used to estimate the mean near-surface currents. Following Lumpkin et al. (2013), an improved technique was used to distinguish drifters that have their drogue attached and follow the ocean currents at 15 m depth with relatively small wind slip from those which have lost their drogue, follow currents nearer the ocean surface, and are subject to larger wind slip. Because of the strong near-surface zonal currents and divergent meridional currents in the equatorial Atlantic, drifters do not typically remain in the region they were deployed and the total number of drifter measurements close to the equator tends to be significantly smaller

than the number of measurements a few degrees poleward of the equator. Thus, simply removing the undrogued drifters from the data set collected in the tropical Atlantic limits the ability to produce a robust estimate of the mean near-surface currents in this region. During the approximately 12-h every 10 days that the Argo floats are at the surface, they essentially behave as an undrogued drifter albeit with different wind-slip characteristics, and utilization of the YoMaHa'07 data set allows for an additional increase in the number of near-surface velocity measurements between 30°W and 8°W and 5°S and 5°N. The Argo float surface drifts, undrogued drifters, and drogued drifters represent 9, 24, and 68 %, respectively, of the total drift measurements in that region.

We have applied a wind-slip correction to both drogued and undrogued drifter as well as Argo float near-surface velocity measurements (Niiler and Paduan 1995; Pazan and Niiler 2001) to combine these three types of measurements and estimate the mean 15-m currents in the central and eastern equatorial Atlantic. This corrected velocity can be expressed as:

$$u_{corrected} = u_{uncorrected} - AW_x$$
$$v_{corrected} = v_{uncorrected} - AW_y,$$

where W_x and W_y are the zonal and meridional component of the wind velocity (in units of m s^{-1}) from NCEP/NCAR Reanalysis v.2 6-hourly winds and the coefficient $A = 7 \times 10^{-4}$ for drogued drifters and $A = 1.64 \times 10^{-2}$ for undrogued drifters. The coefficient for drogued drifters is the same value as used in Niiler and Paduan (1995). However, the undrogued-drifter coefficient was increased from the Pazan and Niiler (2001) value, $A = 8.6 \times 10^{-3}$, to remove a significant westward bias found in the corrected undrogued zonal velocity relative to the corrected drogued zonal velocity in the central and eastern equatorial Atlantic. The coefficient for the Argo float surface drifts, $A = 1.14 \times 10^{-2}$, is very similar to the undrogued value.

To produce mean velocity estimates along 23°W and 10°W at every 0.5° latitude, the slip corrected drifter and Argo data are grouped into 10° (at 23°W) and 4° (at 10°W) longitudinal bins and 1° latitudinal bins. These different longitudinal windows were chosen (1) to ensure sufficient samples (N > 539 drifter-Argo days including 69 float days at 23°W, N > 120 drifter-Argo days including 10 float days at 10°W) along both sections between 5°S and 5°N, and (2) to mirror the larger (7°) spread in longitudes for the cruises conducted primarily along 23°W. Within those bins, the observations are treated as time series that are fit via least-squares regression to a model composed of a time-mean value, annual and semiannual harmonics, and linear trends corresponding to the longitudinal and latitudinal distance from the bin center. This minimizes the influence of seasonal and spatial sampling biases on the combined drifter and Argo mean velocity estimates within each bin. It must be noted that some of the six-hourly drifter measurements collected within each bin may not independent from one another, and the Argo surface float measurements are obtained approximately over a 12-h period every 10 days and may alias high-frequency motions. Given that these caveats would alternately require downweighting the drifter and Argo surface float data relative to one another, we have decided to combine them both without any downweighting.

Constant vertical shear is assumed in the upper 30 m to linearly extrapolate the long-term mean ship-based ADCP velocity (Sect. 2.1) upwards to the surface (similar to Brandt et al. 2006 and subsequent studies). This constant shear is set by the vertical gradients between the 30-m mean ADCP and the 15-m mean drifter-Argo velocities, and the resulting volume transport in the upper 30 m is equivalent to the volume transport by a well-mixed surface layer with flow in the upper 30 m given by the 15-m mean drifter-Argo velocity (i.e., zero shear). The resulting mean meridional velocity sections will hereafter be referred to as "ADCP+D". Like previous studies (Molinari et al. 2003; Brandt et al. 2010), we assume that the mean velocity measurement error is small compared to the error of the mean velocity due to geophysical noise, such as those from TIWs and other mesoscale phenomena. Thus, below 30 m depth, uncertainties of the ADCP+D means are estimated by the standard error of the mean ship-based ADCP velocity which is given by the observed standard deviation divided by the square root of the number of samples. Above 30 m, the uncertainties are determined by adding white Gaussian noise on the order of the standard error for the mean near-surface velocity estimates to the combined drifter and Argo data prior to vertical extrapolation—1,000 such simulations were run and twice the standard deviation (or 2-σ value) of those realizations was used to provide the 95 % confidence intervals.

2.3 OSCAR product

Additionally, the long-term mean ship-based ADCP velocity is vertically extrapolated to the surface using the publically-available Ocean Surface Current Analysis Real time (OSCAR) product (e.g., Bonjean and Lagerloef 2002) often used to study the tropical Atlantic circulation (e.g., Helber et al. 2007; Da-Allada et al. 2013). OSCAR provides an independent estimate of the depth-averaged velocity in the upper 30 m of the water column computed from remotely sensed sea surface height (SSH), surface winds, sea surface temperature (SST), and mean dynamic height topography using Ekman, geostrophic, and Stommel shear dynamics. For this study, we use the (spatially filtered) 1° gridded OSCAR product from January 1, 1993 to

December 31, 2011, which is available as 5-day averages (e.g., Helber et al. 2007; Da-Allada et al. 2013). The mean ship-based ADCP velocity is then extrapolated to the surface in the same manner as for the combined drifter and Argo data, that is assuming constant vertical shear between the 30-m mean ADCP and the mean OSCAR velocities—hereafter referred to as "ADCP+O". This provides a means to examine the differences in the mean cross-equatorial and vertical structure of meridional velocity that result from applying a different near-surface velocity product.

2.4 Moored current measurements

Independent current observations from moored ADCPs in the central and eastern equatorial Atlantic (Fig. 1) are also used to evaluate the mean ADCP+D currents in the upper 300 m of the water column. Moored ADCP velocity measurements are available along 23°W at 2°S, 0.75°S, 0°, 0.75°N, and 2°N, as well as along 10°W at 0.75°S, 0°, and 0.75°N as daily or 12-hourly averages. The moored ADCP measurements resolve the currents from 15 m (only at equatorial moorings) to 50 m down to an intermediate depth (most commonly 300 m), with vertical range and resolution dependent on factors such as configuration and instrument depth (e.g., Provost et al. 2004; Brandt et al. 2006, 2008; Bunge et al. 2007; Kolodziejczyk et al. 2009). Daily averages from single point current meters mounted on the 23°W, 0°—PIRATA backbone mooring at 10 m depth (and 20 m depth during 2008–2009) and the 23°W, 4°N—PNE mooring at 10 m depth (Fig. 1) provide the only other concurrent time series of velocity in the region above 20 m. Similar to the combined drifter and Argo data (Sect. 2.2), the moored velocity observations are fit via least-squares regression to a model composed of a time-mean value, and annual and semiannual harmonics. The seasonal cycle is then removed from the moored data prior to estimating their means to account for potential seasonal sampling biases in the mooring records. Note, due to the only 1-year 20-m current meter record at the 23°W, 0°—PIRATA mooring, the seasonal cycle from the moored ADCP data at that depth and location is used to correct for seasonal biases.

The uncertainties of the mean moored velocities are estimated by their standard errors which are given by the standard deviation divided by the square root of the total number of degrees of freedom, or the total number of days divided by twice the decorrelation time scale. At the moorings, the decorrelation time scale is usually between 7 and 10 days for meridional velocity which corresponds to about 1/4–1/2 of a typical TIW period. This error does not account for the estimated compass uncertainty of ±2° for the moored ADCPs and ±5° for the fixed-depth current meters (Freitag et al. 2003; Plimpton et al. 2004), which leads to a systematic meridional velocity bias for each deployment of approximately ±4 and ±9 %, respectively, of the absolute measured velocity. As the orientation of the compass error is random for each instrument, the impact of the compass errors decreases as the number of mooring deployments increase. The total error of the moored meridional velocity is then given by the square root of the sum of the square of the compass error divided by the number of mooring deployments (between 1 and 6 deployments), and the square of the standard error. For the data sets considered here, the magnitude of the compass errors can be as large as 1.5 cm s^{-1} at the depth of the EUC core for the 0.75°S, 0°, and 0.75°N ADCP moorings, and smaller than 1 cm s^{-1} for all of the fixed-depth current meters and other ADCP moorings.

2.5 Reanalysis product

Output from one of the GLobal Ocean ReanalYsis and Simulations (GLORYS; Ferry et al. 2010) products is also used to evaluate the mean meridional currents estimated from ADCP+D, ADCP+O, and mooring data along 23°W and 10°W. The GLORYS project is a cooperative initiative between Mercator Océan and the French research community to provide a series of eddy permitting global ocean simulations, based on version 3.1 of the Nucleus for European Models of the Ocean (NEMO) modeling system (Barnier et al. 2006; Madec 2008). Model equations are discretized using the standard ORCA025 configuration which has a tri-polar grid, with nominal horizontal resolution of 1/4° at the equator. The model has 75 vertical levels, with approximately 1-m resolution near the surface and 200-m resolution in the deep ocean. The version of GLORYS used in this study, GLORYS2V1, is forced with ECMWF ERAInterim forcing fields (Simmons et al. 2007). GLORYS2V1 assimilates remotely sensed SST and SSH information, mean dynamic topography, and in situ temperature and salinity data from December 4, 1992 to December 31, 2009 via a reduced order Kalman filter (Pham et al. 1998; Tranchant et al. 2008) and a double backward incremental analysis technique (Bloom et al. 1996; Benkiran and Greiner 2008).

PIRATA and PNE temperature and salinity data are assimilated by GLORYS2V1, and as a result there is good agreement on intraseasonal to interannual time scales between the 10-m temperature and salinity observations and the global reanalysis at those sites. For example, at 0° and 4°N along 23°W, biases of less than 0.13 °C for temperature and 0.10 psu for salinity, and correlations greater than 0.89 for temperature and 0.61 for salinity are found (Tables 1, 2). Although in situ velocity measurements are not assimilated, GLORYS2V1 produces

Table 1 Comparison of observed 10-m temperature, salinity, zonal and meridional velocity at the 0°, 23°W-PIRATA mooring site for the days of overlap with the GLORYS2V1 simulation during May 29, 2005 to December 31, 2009

Field	Mean difference	Correlation	Record length (days)
Temperature	0.13 (0.13) °C	0.96 (0.81)	1637
Salinity	0.09 (0.11) psu	0.62 (0.52)	1224
Zonal velocity	10.24 (8.41) cm s^{-1}	0.71 (0.60)	942
Meridional velocity	−0.50 (−0.86) cm s^{-1}	0.57 (0.57)	942

The start date corresponds to the date when the mooring was augmented with the 10-m fixed-depth current meter. The means of the PIRATA minus GLORYS2V1 fields are given, as well as their correlation and the total number of days of overlap. The seasonal cycle has been removed for the values provided in parenthesis. Correlations are all significant above the 99 % confidence level

Table 2 Comparison of observed 10-m temperature, salinity, zonal and meridional velocity at the 4°N, 23°W-PNE mooring site for the days of overlap with the GLORYS2V1 simulation during June 11, 2006 to December 31, 2009

Field	Mean difference	Correlation	Record length (days)
Temperature	−0.01 (−0.05) °C	0.89 (0.84)	1064
Salinity	0.10 (0.13) psu	0.61 (0.58)	889
Zonal velocity	−1.51 (−1.30) cm s^{-1}	0.54 (0.50)	915
Meridional velocity	2.31 (0.19) cm s^{-1}	0.53 (0.53)	915

The start date corresponds to the mooring deployment date. The means of the PNE minus GLORYS2V1 fields are given, as well as their correlation and the total number of days of overlap. The seasonal cycle has been removed for the values provided in parenthesis. Correlations are all significant above the 99 % confidence level

relatively unbiased currents that are significantly correlated (with correlations between 0.53 and 0.71) with the available moored 10-m velocity data at 0° and 4°N along 23°W. Note, the biases and correlations computed after the seasonal cycle has been removed (parentheses in Tables 1, 2), demonstrate that the skill is not just due to the model correctly reproducing the seasonal cycle.

3 Results

3.1 Cross-equatorial structure of meridional currents

Figure 4 shows the distribution of the long-term mean meridional currents from ADCP+D along 23°W and 10°W, and compares with GLORYS2V1 meridional currents averaged from January 1, 1993 to December 31, 2009. The number of ship-based ADCP samples and the uncertainties estimated for the ADCP+D long-term means are presented in Fig. 5 (see Sect. 2.2). At the surface, maximum mean poleward flow of −7.6 cm s^{-1} is observed at 1.50°S and 13.9 cm s^{-1} at 2.05°N along 23°W (Fig. 4a). Similarly, maximum mean poleward flow of −16.4 cm s^{-1} is observed at 3.55°S and 15.2 cm s^{-1} at 0.50°N along 10°W (Fig. 4b). The observed poleward surface currents in Fig. 4a, b are consistent with the expected mean wind-driven currents in the surface limb of the TCs based on previous studies in the western equatorial Atlantic and the central equatorial Pacific (e.g., Johnson et al. 2001; Molinari et al. 2003; Perez et al. 2010). The thickness of the poleward flow in the surface limb is approximately 30 m in the northern cell and 50 m in the southern cell, consistent with the mean thermocline or pycnocline depth north of 3°S being at least 10 m shallower than south of 3°S (e.g., Brandt et al. 2006, 2010; Kolodziejczyk et al. 2009). As a result of the shallower northern cell, the presence of mean northward flow north of the equator in the surface limb is more heavily constrained by the vertical extrapolation to the drifter-Argo data (discussed further in Sect. 3.2). The boundary between the surface limb of the northern and southern cells is south of the equator along both longitudes: It is found near 0.35°S along 23°W while it occurs near 1.05°S along 10°W. This off-equatorial location of the transition between the cells has been previously observed from shipboard meridional velocity observations in the western equatorial Atlantic (Molinari et al. 2003) and is consistent with maximum equatorial divergence being found approximately 1° south of the equator in observations and models (e.g., Molinari et al. 2003; Helber et al. 2007; Giordani and Caniaux 2011).

Below the surface limb, the southward flow north of the equator along 23°W has several local maxima that are part of a broad subsurface equatorward flow between 1°N and 5°N, with strongest flow of −5.9 cm s^{-1} centered at 3.55°N and a depth of 40 m (Fig. 4a). This subsurface equatorward flow in the northern hemisphere is less broad in its meridional extent but stronger in magnitude along 10°W, with maximum southward flow of −8.7 cm s^{-1} at 1.6°N and a depth of 50 m (Fig. 4b). Subsurface northward flow is found in the southern hemisphere along 23°W, with maximum velocity of 3.6 cm s^{-1} centered at 1.25°S and a depth of 80 m (Fig. 4a). In contrast, strong southward flow is found in the southern hemisphere along 10°W between 2°S and the equator reaching −11.8 cm s^{-1} at 0.9°S and 40 m depth, with weaker northward flow only between 4°S and 2°S (Fig. 4b). The abrupt nature of this shift from northward to southward flow at 2°S along 10°W is likely due to a significant reduction in the number of samples south of 2°S (Fig. 5b).

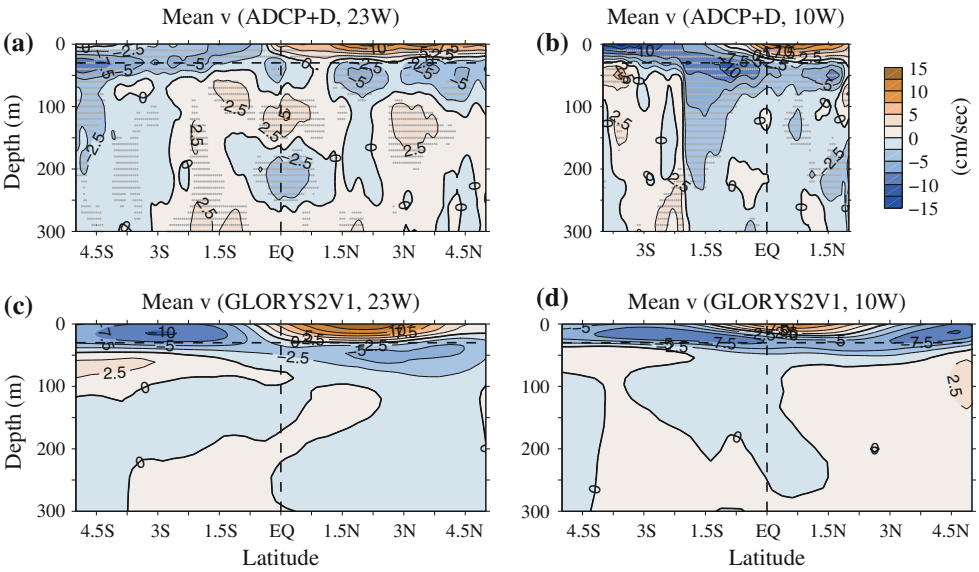

Fig. 4 Distribution of long-term mean **a**, **b** observed (ADCP+D) and **c**, **d** GLORYS2V1 meridional velocity along 23°W and 10°W. Mean observed velocity below 30 m (*black horizontal dashed line*) is derived from all available ship-based ADCP measurements (Fig. 1b), and mean velocity above 30 m is vertically extrapolated to mean drifter-Argo velocities (see Sect. 2.2 for details). *Gray dots* in (**a**, **b**) indicate statistically significant values. Contour interval is 2.5 cm s^{-1}

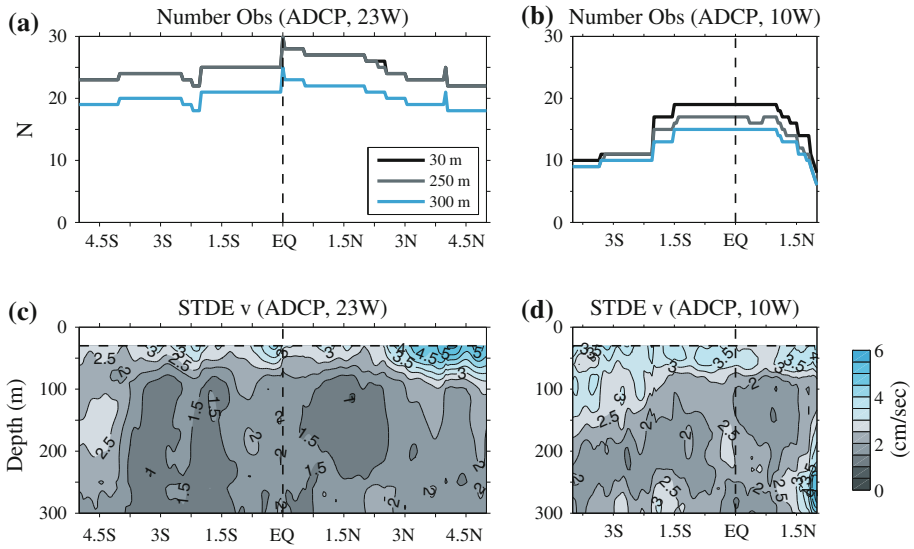

Fig. 5 Plot of **a**, **b** the number of ADCP sections, and **c**, **d** the distribution of the standard errors of the ship-based ADCP meridional velocity for all available ship-based ADCP measurements along 23°W and 10°W. *Upper panels* show the number of samples at depths of 30 m (*black line*), 250 m (*gray line*), and 300 m (*blue line*). Contour interval is 0.5 cm s^{-1} for *lower panels*

The mean meridional-vertical structure of the currents from GLORYS2V1 (Fig. 4c, d) agrees well with the observed structure in the upper 30 m (Fig. 4a, b), with stronger poleward velocities north of the equator than south of the equator (14.6 cm s^{-1} compared with −8.3 cm s^{-1} along 23°W, and 10.8 cm s^{-1} compared with −7.7 cm s^{-1} along 10°W), a thinner surface limb in the northern cell than in southern cell along both longitudes, and a southward shift of the northern cell maxima as well as of the boundary between the northern and southern cells between 23°W and 10°W. Near the equator, the observed and GLORYS2V1 subsurface flow structures below 30 and 100 m bear little resemblance to one another. However, poleward of ±2° latitude, the simulated subsurface equatorward flow in that depth range has much in common with the observed flow. Although the weak mean meridional currents below the TCs in the observations and GLORYS2V1 share some common elements in the southern hemisphere (e.g., the transition from northward to southward flow near 2°S along 10°W in Fig. 4b, d), there is no overall agreement below 100 m in the northern hemisphere.

The observed volume transport associated with the mean TCs,

$$\bar{V}_{\text{int}}(y,-D) = \int_{23\text{W}}^{10\text{W}} \int_{-D}^{0} \bar{v}(x,y,z)\,dz\,dx,$$

is estimated by averaging the mean ADCP+D meridional velocity ($\bar{v}$) along 23°W and 10°W, multiplying by their 13°-longitude separation, and integrating over the thickness D of the upper branch of the cell,

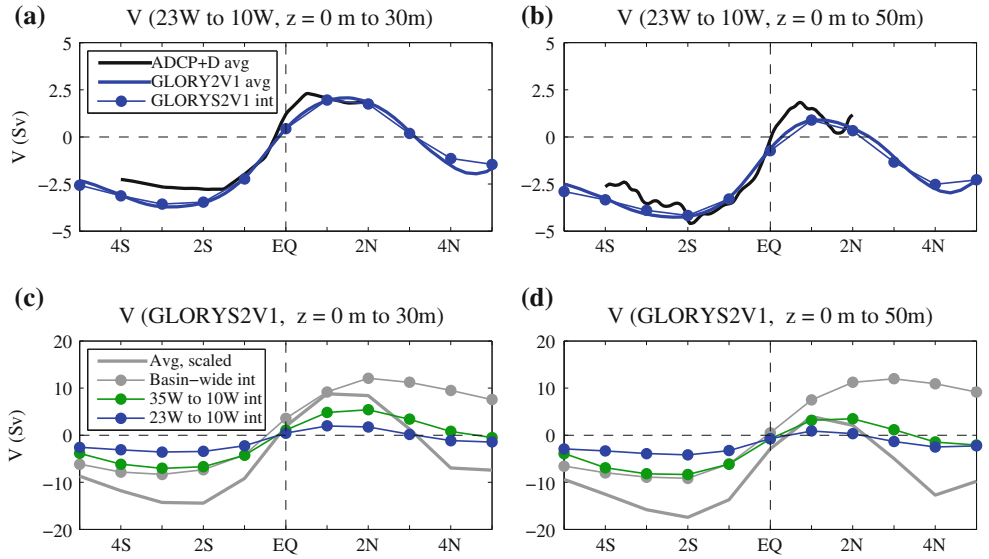

Fig. 6 Comparison of long-term mean meridional volume transport integrated from 0 to 30 m (*left*) and 0 to 50 m (*right*). **a**, **b** Meridional transport between 23°W and 10°W estimated from the average of mean ADCP+D (*thick black lines*) and simulated (*thick blue lines*) velocities along 23°W and 10°W, with the zonally-integrated simulated velocity (*blue lines with circles*) overlaid at selected latitudes. **c**, **d** Comparison of the GLORYS2V1 meridional transport zonally integrated between 23°W and 10°W (*blue lines with circles*), 35°W and 10°W (*green lines with circles*), and across the basin (*gray lines with circles*) at selected latitudes, with the transport computed from the average of mean GLORYS2V1 velocities along 23°W and 10°W and scaled by the size of the basin (*thick gray lines*) overlaid

$$\bar{V}_{avg}(y,-D) = \frac{13}{2} \times (111\text{km}\cos\theta) \int_{-D}^{0} (\bar{v}(23\text{W},y,z) + \bar{v}(10\text{W},y,z))dz,$$

where θ *is latitude*. The observed meridional transport in the surface limb of the southern cell is larger than the transport in the surface limb of the northern cell. This is apparent from Fig. 6a, b showing the observed meridional transport (black thick lines) in the top $D = 30$ m and D = 50 m, respectively, which correspond to the mean thicknesses of the surface limb of the northern and southern cells. North of the equator maximum northward transport of 2.3 Sv (1 Sv = 10^6 m^3 s^{-1}) is found at 0.55°N in a 30-m thick layer (Fig. 6a), while south of the equator maximum southward transport of −4.6 Sv occurs at −1.95°S in a 50-m thick layer (Fig. 6b).

The simulated meridional volume transports associated with the mean TCs, estimated from the average of the mean GLORYS2V1 meridional velocity along 23°W and 10°W, are very similar to the observed values (compare blue and black thick lines in Fig. 6a, b), with maximum simulated northward transport of 2.1 Sv at 1.35°N for a 30-m thick layer (Fig. 6a), and maximum simulated southward transport of −4.3 Sv at −2.35°S for a 50-m thick layer (Fig. 6b). Note, whether the transport is estimated by zonally integrating the mean GLORYS2V1 meridional velocity at all model grid points between 23°W and 10°W ($\bar{V}_{\text{int}}$, blue lines with circles) or just by averaging the meridional velocity along 23°W and 10°W and multiplying by their 13°-longitude separation ($\bar{V}_{avg}$, thick blue lines), the simulated transports are nearly identical. This suggests that the meridional volume transport varies linearly in longitude between 23°W and 10°W.

Despite the limited observational data, we note that the range and structure in the observed variability of the meridional currents along 23°W and 10°W (Fig. 7a, b) is quite similar to the range and structure of the simulated variability (Fig. 7c, d). The variability is largest near the surface, with standard deviations at 30 m depth ranging between 10 and 27 cm s^{-1} for the ADCP data and between 12 and 20 cm s^{-1} for GLORYS2V1. For both the model and observations, the variability associated with the mean position of the northern cell tends to be larger than that of the southern cell, and the region of high variability below the surface limb of the northern cell extends deeper along 23°W (Fig. 7a, c) than along 10°W (Fig. 7b, d). The equatorial asymmetry in the variability of meridional velocity is primarily due to the asymmetric wind forcing in the region associated with the seasonal migration of the Intertropical Convergence Zone (ITCZ) complex (e.g., Helber et al. 2007), and secondarily due to asymmetric TIW and submonthly-to-intraseasonal wind-forced variability (e.g., Athié and Marin 2008; Athié et al. 2009; Perez et al. 2012).

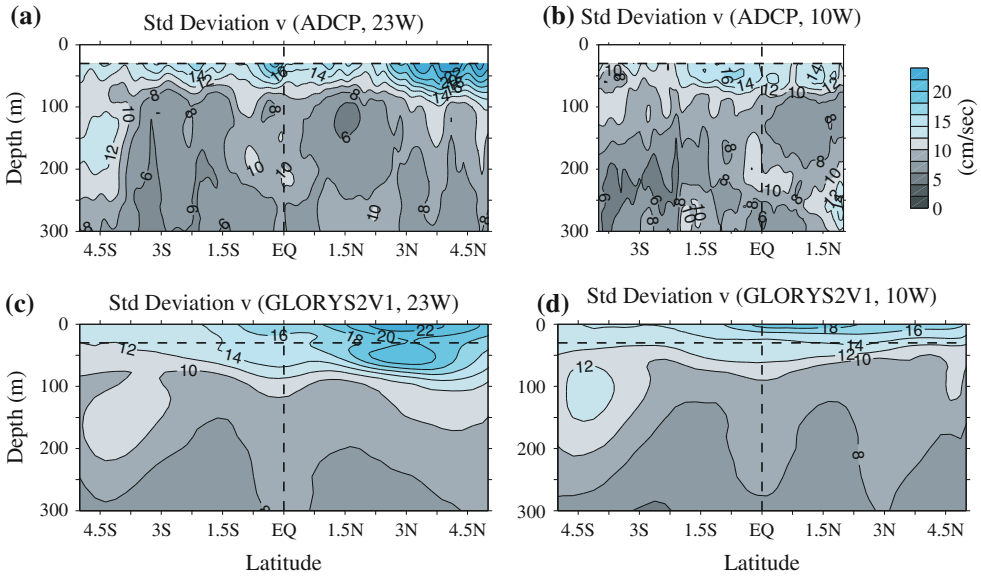

Fig. 7 Distribution of the standard deviation of **a**, **b** ship-based ADCP for all available ship-based ADCP measurements and **c**, **d** GLORYS2V1 meridional velocity along 23°W and 10°W. Contour interval is 2 cm s^{-1}

Since the number of samples is fairly constant between 5°S and 5°N along 23°W and between 2°S and 2°N along 10°W (Fig. 5a, b), the meridional-vertical structure of the ADCP standard errors (Fig. 5c, d) bears a strong resemblance to that of the ADCP standard deviations (Fig. 7a, b), and the largest uncertainties in the mean estimates are generally found in the regions of high variability. Standard errors are typically between 2 and 6 cm s^{-1} above 100 m depth, and smaller than 2 cm s^{-1} below 100 m depth except poleward of about ±2° latitude along 10°W due to the large drop in the number of samples (Fig. 5b).

3.2 Comparisons at discrete depths and mooring locations

For both longitudes, the mean ship-based ADCP meridional velocity blended with the mean near-surface velocity from the drifter-Argo data (ADCP+D) at 10 m (Fig. 8a, b) and 20 m (Fig. 8c, d) depth is compared with the mean ship-based ADCP meridional velocity blended with the mean OSCAR fields (ADCP+O), mean meridional velocities estimated from moored observations in the upper 20 m (see Fig. 1; Sect. 2.4), and the mean GLORYS2V1 meridional velocities. The meridional structure of the mean ADCP+D meridional velocities (solid black lines) generally agrees well with that of the mean GLORYS2V1 meridional velocities (blue lines). However, the simulated magnitudes can be as much as 5 cm s^{-1} larger than the observed magnitudes along 23°W (Fig. 8a, c), and as much as 5 cm s^{-1} smaller than the observed magnitudes north of the equator along 10°W (Fig. 8b, d). The ADCP+D, ADCP+O (dashed black lines), and GLORYS2V1 currents overlap within the uncertainty with the relatively weak mean meridional velocities estimated from the moored observations at 0°N and 4°N along 23°W (green and red circles in Fig. 8a, c). Unfortunately, moored velocity measurements are not available where the three estimates disagree the most within the latitudes of maximum poleward flow associated with the TCs (typically between ±1° and ±4° latitude).

In general, large differences are found between mean ADCP+D and ADCP+O meridional velocities at both depth levels. For example, the maximum poleward flow in ADCP+D is approximately 5 cm s^{-1} larger in magnitude than in ADCP+O along 23°W and 10°W at 10 m depth (Fig. 8a, b), and even differs in sign from the ADCP+D velocity in the southern cell. The biased representation of the mean near-surface meridional currents in ADCP+O is consistent with a recent qualitative comparison by Da-Allada et al. (2013) of the previous version of the mean drifter annual climatology (Lumpkin and Garraffo 2005; Lumpkin and Garzoli 2005) and OSCAR velocities, suggesting that OSCAR mean meridional velocities do not adequately constrain the near-surface poleward flow in the central and eastern equatorial Atlantic. Note, if instead of extrapolating to these near-surface velocity products, the mean vertical shear between 30 m and 40 m depth from the ship-based ADCP meridional velocity is used to extrapolate upwards as in previous studies (e.g., Johnson et al. 2001; Schott et al. 2003), the mean surface flow would be on the order of 5 cm s^{-1} weaker along 10°W, and would be oriented southward rather than northward along 23°W (not shown). Thus, the mean vertical shear between 30 m and 40 m depth is also insufficient to adequately constrain the near-surface poleward flow.

At the nine sites along 23°W and 10°W between 2°S and 4°N where moored current measurements are available (Fig. 1; Sect. 2.4), the mean ADCP+D meridional velocity

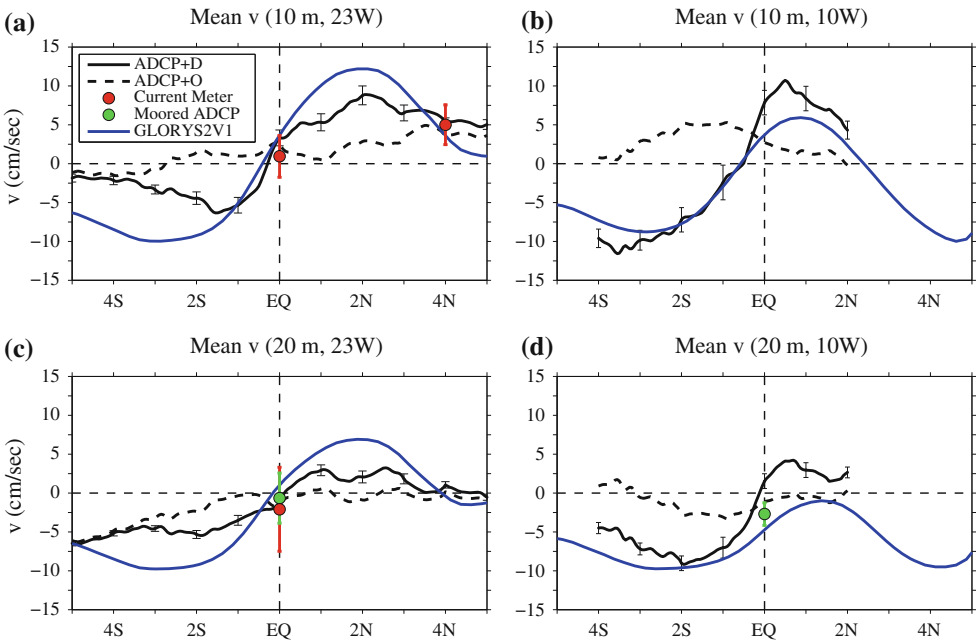

Fig. 8 Comparison of long-term mean ship-based ADCP meridional velocity vertically extrapolated to the drifter-Argo (ADCP+D, *solid black lines*) and OSCAR surface velocities (ADCP+O, *dashed black lines*) at **a**, **b** 10 m and **c**, **d** 20 m depth along 23°W (*left*) and 10°W (*right*). Mean GLORYS2V1 meridional velocity is overlaid in *blue*. Mean meridional velocity derived from moored fixed-depth current meters is indicated by *red circles* and from moored ADCPs by *green circles*. *Error bars* denote the 95 % confidence limits for the ADCP+D data and the total errors for the moored measurements

as well as the mean GLORYS2V1 meridional velocity can be further evaluated in the upper 300 m (Fig. 9). The mean moored ADCP meridional velocities (thick green lines) typically agree quite well with the mean ship-based ADCP meridional velocities (thick black lines) and overlap within the standard errors for each of those estimates. Exceptions are at the equator and 0.75°N along 23°W between about 75 and 150 m depth where the ship-based ADCP estimate exhibits too strong northward flow in the EUC core region (Fig. 9c, d), and at 0.75°S along 10°W between 50 and 100 m where the flow is too strong southward (Fig. 9g). At the 0°–23°W mooring, the ship-based ADCP estimate also exhibits too strong southward flow below the EUC between 150 and 250 m (Fig. 9c), suggesting that there are not enough ship sections to average out the mesoscale variability near the equator between 50 and 250 m. At most sites, the mean GLORYS2V1 meridional velocities (thick blue lines) are in good agreement with both the mean moored ADCP and the fixed-depth current meter (red circles) velocity estimates, with the exception of too weak southward flow at the equator and 0.75°N along 10°W in the EUC core region between 50 and 150 m depth (Fig. 9h, i).

3.3 Seasonal comparison

The seasonal distribution of the ADCP sections (Fig. 3; Sect. 2.1) provides an opportunity to examine the meridional-vertical structure of mean meridional velocity associated with the TCs during Dec–May and Jun–Nov along 23°W (Fig. 10) and compare with the 6-month mean drifter-Argo and GLORYS2V1 meridional velocities (Figs. 10, 11). Although there are not enough ADCP sections along 10°W to similarly partition the ship-based ADCP meridional velocities into Dec–May and Jun–Nov averages, the 6-month mean drifter-Argo and GLORYS2V1 meridional velocities can be examined along 10°W (Fig. 12a–d). For this reason, we do not combine the 6-month mean ship-based ADCP meridional velocities with the 6-month mean drifter-Argo meridional velocity estimates along 23°W, but consider the two data sources separately (cf. Figs. 10a, b, 11a, b). The 6-month mean meridional velocities from the moored ADCPs and fixed-depth current meters at the nine sites along 23°W and 10°W (Fig. 14) are also compared with the 6-month GLORYS2V1 means at those locations (Fig. 15). Note that the 6-month mean drifter-Argo and mooring estimates are generated using the harmonic fits to the data described in Sects. 2.2 and 2.4, respectively, rather than from the data solely in those months to reduce sampling biases.

Above 30 m depth, the mean GLORYS2V1 and drifter-Argo poleward flow associated with the upper limb of the TCs along 23°W is stronger during Dec–May than Jun–Nov (Figs. 10c, d, 11a–d). This is consistent with previous findings by Helber et al. (2007) in their seasonal analysis of OSCAR surface velocities (cf. their Fig. 5), although the magnitude of the drifter-Argo seasonal differences is much larger than the OSCAR seasonal differences. The GLORYS2V1 hydrographic fields show large seasonal variations in the zonal temperature gradients north of the equator along 23°W (not shown) which set the strength of the geostrophic component of the meridional velocity, v_g. Using equatorial geostrophy (e.g., Perez and Kessler 2009, and references therein) to obtain estimates of v_g relative to

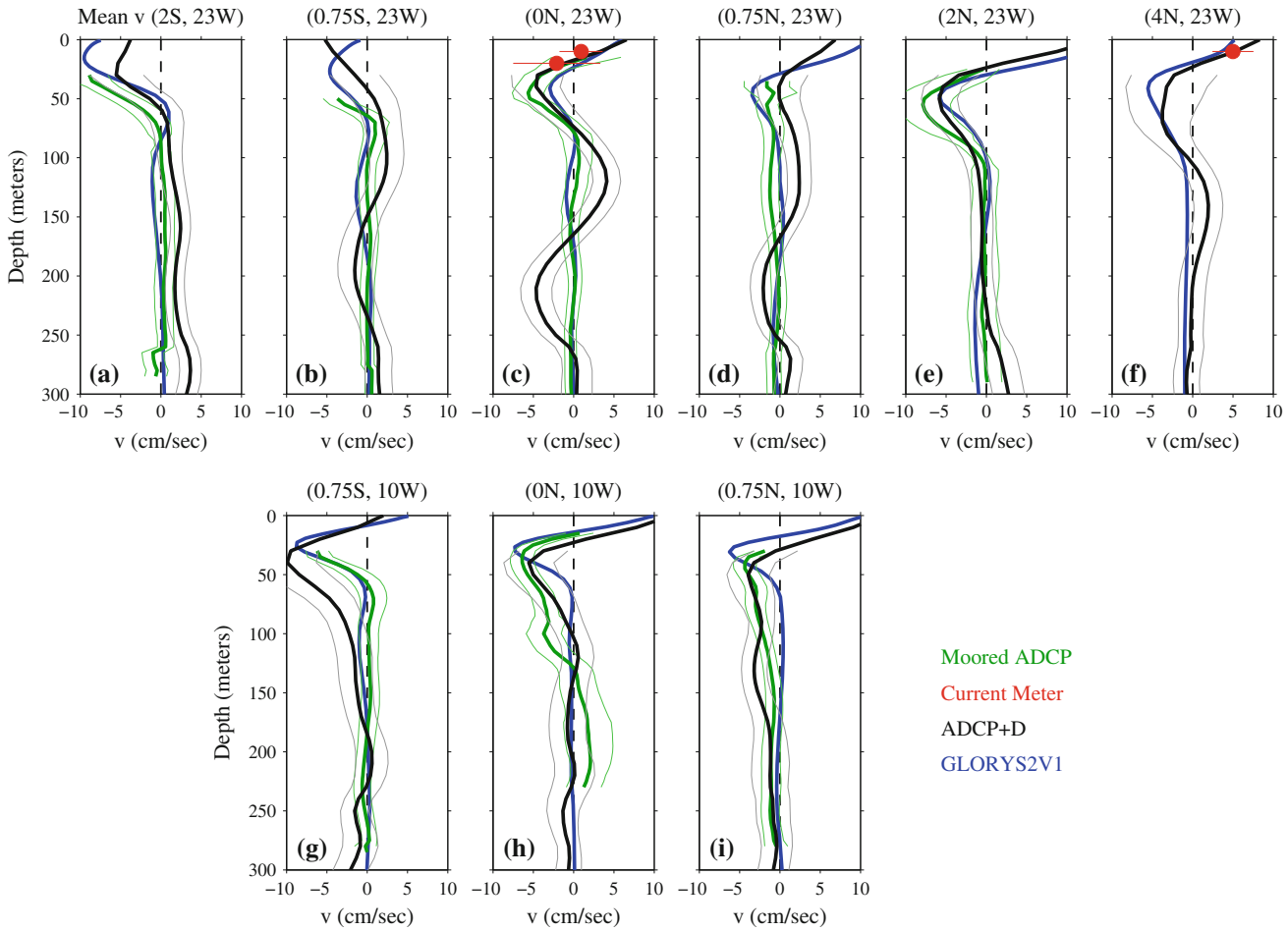

Fig. 9 Comparison of long-term mean ADCP+D meridional velocity (*thick black lines*) at various latitudes along **a**–**f** 23°W and **g**–**i** 10°W. Mean GLORYS2V1 meridional currents are overlaid in *blue*. Mean meridional velocity derived from moored fixed-depth current meters is indicated by *red circles* and from moored ADCPs by *thick green lines*. *Thin lines* denote the means ± standard errors for the ADCP+D and means ± total errors for the moored ADCP measurements, and the *circles* with error bars denote the means ± total errors for the fixed-depth current meter measurements

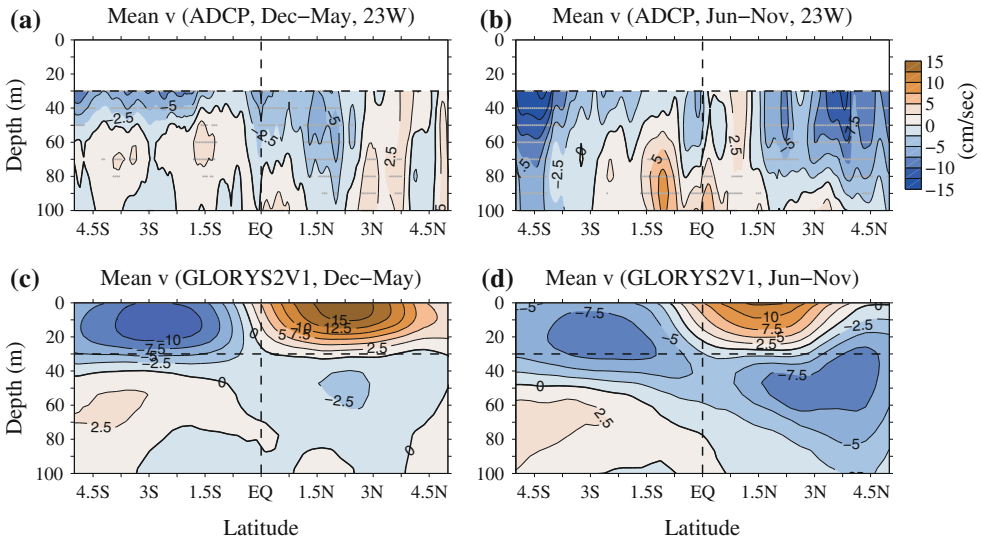

Fig. 10 Distribution of two-season mean **a**, **b** ship-based ADCP and **c**, **d** GLORYS2V1 meridional velocity along 23°W during Dec–May (*left*) and Jun–Nov (*right*). *Gray dots* in (**a**–**b**) indicate statistically significant values. Contour interval is 2.5 cm s^{-1}

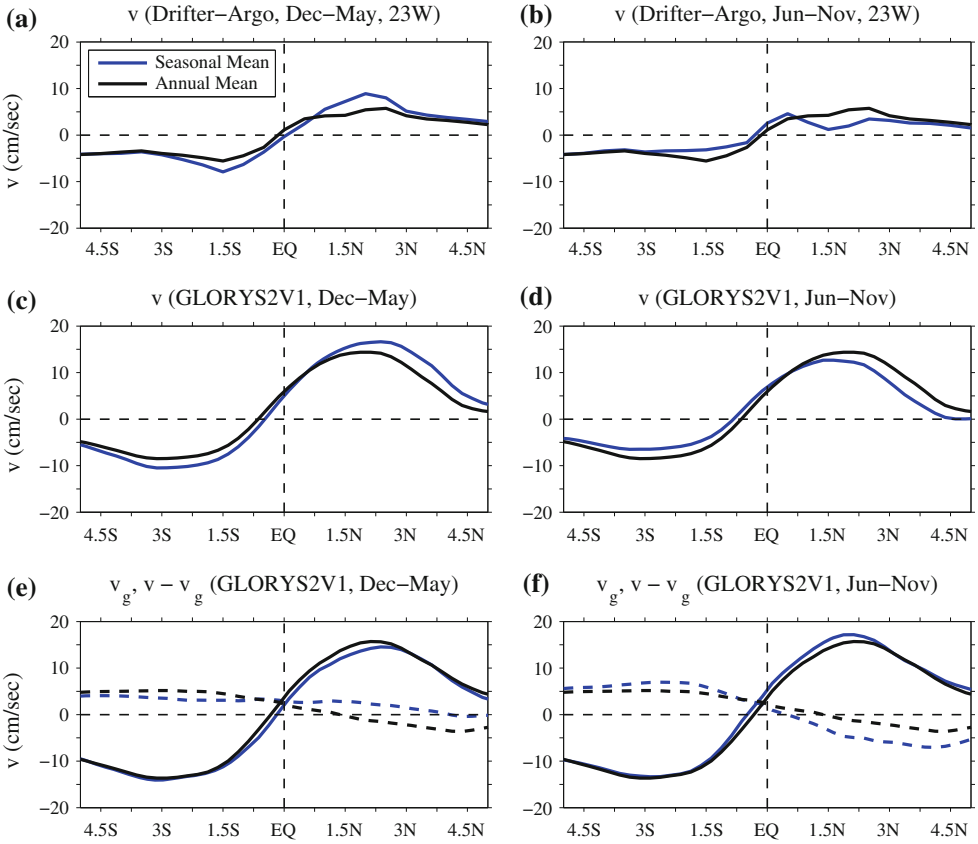

Fig. 11 Comparison of two-season mean near-surface **a**, **b** drifter-Argo and **c**, **d** GLORYS2V1 meridional velocity along 23°W during Dec–May (*left*) and Jun–Nov (*right*). *Panels* **e**, **f** show the simulated equatorially-modified geostrophic component of the meridional velocity, v_g, computed using the GLORYS2V1 sea surface height (*dashed lines*), and the ageostrophic component of meridional velocity, $v_{ag} = v - v_g$ (*solid lines*). For comparison, the long-term means are plotted in *black* and seasonal means are plotted in *blue*

an assumed level of no motion at the sea floor from the GLORYS2V1 SSH fields, reveals that there is northward geostrophic flow north of the equator along 23°W in Dec–May and southward geostrophic flow in Jun–Nov (dashed blue lines in Fig. 11e, f). At this longitude, the seasonal variability of the geostrophic component is larger than the seasonal variability of the ageostrophic component of meridional velocity (v_{ag}, solid blue lines in Fig. 11e, f), computed simply as the residual between the total near-surface velocity (Fig. 11c, d) and v_g, and thus more strongly influences the seasonality of the total near-surface velocity. In contrast, the maximum near-surface northward flow in the northern cell along 10°W occurs during Jun–Nov for the drifter-Argo and GLORYS2V1 meridional velocities (Fig. 12a–d), consistent with the stronger seasonal variability of the near-surface ageostrophic component of meridional velocity between 1°S and 2°N along 10°W (Fig. 12e, f).

The observed and GLORYS2V1 mean southward displacement between the northern and southern cells, and the southward shift of the boundary from Dec–May to Jun–Nov, is due to the asymmetric structure of v_{ag}, and to a lesser extent v_g (Figs. 11, 12). The equatorially asymmetric structure of the annual and seasonal mean v_{ag} is consistent with the asymmetric structure of the mean wind-driven component of the near-surface meridional velocity. This can be qualitatively seen from the wind-driven component of meridional transport estimated using the simple equatorially-modified Ekman model applied by Perez et al. (2012) and the GLORYS2V1 surface zonal and meridional wind stress (τ_x, τ_y):

$$V_{ek} = \frac{r_s \tau_y - f \tau_x}{\rho_0 (f^2 + r_s^2)},$$

where ρ_0 is seawater density, f is the Coriolis parameter, and $r_s = (1.5\ \text{day})^{-1} \sim f$ at 3°N is the vertical shear dissipation rate. From the above equation, the location of the boundary between northward and southward wind-driven transport can be derived as the latitude where $V_{ek} = 0$ or $f = r_s \tau_y / \tau_x$ (note, this latitude varies linearly with the choice of r_s). For the prevailing southeasterly winds along 23°W, the long-term mean boundary between the northward and southward wind-driven transport lies at 1.70°S (black line in Fig. 13a). Along 10°W, the winds become more southerly, shifting the boundary between the northward and southward wind-driven transport further southward to 3.15°S (black line in Fig. 13c). Seasonal variations in the winds also appear to be partly responsible for the observed and simulated southward shift of the boundary between the northern and southern cells from Dec–May (Fig. 13a, c) to Jun–Nov (Fig. 13b, d).

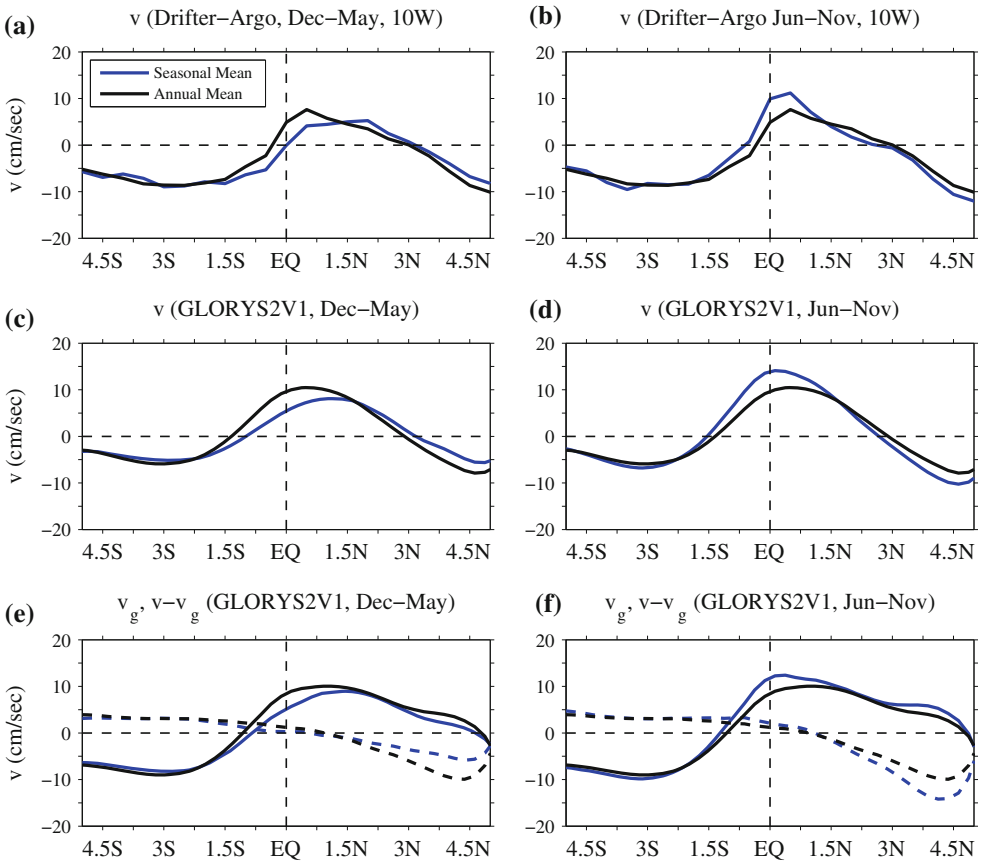

Fig. 12 Same as Fig. 11, except along 10°W

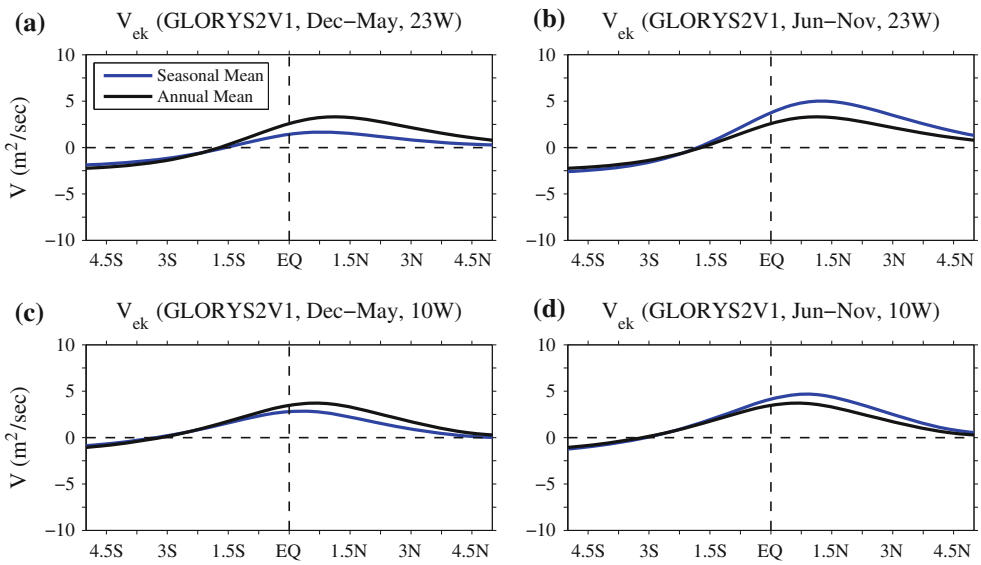

Fig. 13 Comparison of two-season mean equatorially-modified Ekman meridional transport computed using the GLORYS2V1 surface wind stress along **a**, **b** 23°W and **c**, **d** 10°W. For comparison, the long-term means are plotted in black and seasonal means are plotted in *blue*

Below 30 m depth, the winds exert less influence upon the meridional currents and this compensation between the seasonal variations of v_g and v_{ag} does not occur. Although there are some differences between the 6-month mean ship-based ADCP (Fig. 10a, b) and GLORYS2V1 (Fig. 10c, d) meridional velocities along 23°W which may not be significant given the large observed standard errors, both indicate seasonal strengthening of the equatorward flow in the lower limb of the TCs between 1.5°N and 5°N in the northern cell, and to a lesser extent between 3°S and the equator in the southern cell during Jun–Nov (Fig. 10). The stronger southward flow between 1.5°N and 5°N in the lower limb of the northern cell during Jun–Nov also occurs along 10°W in GLORYS2V1 (not shown). Analysis of the

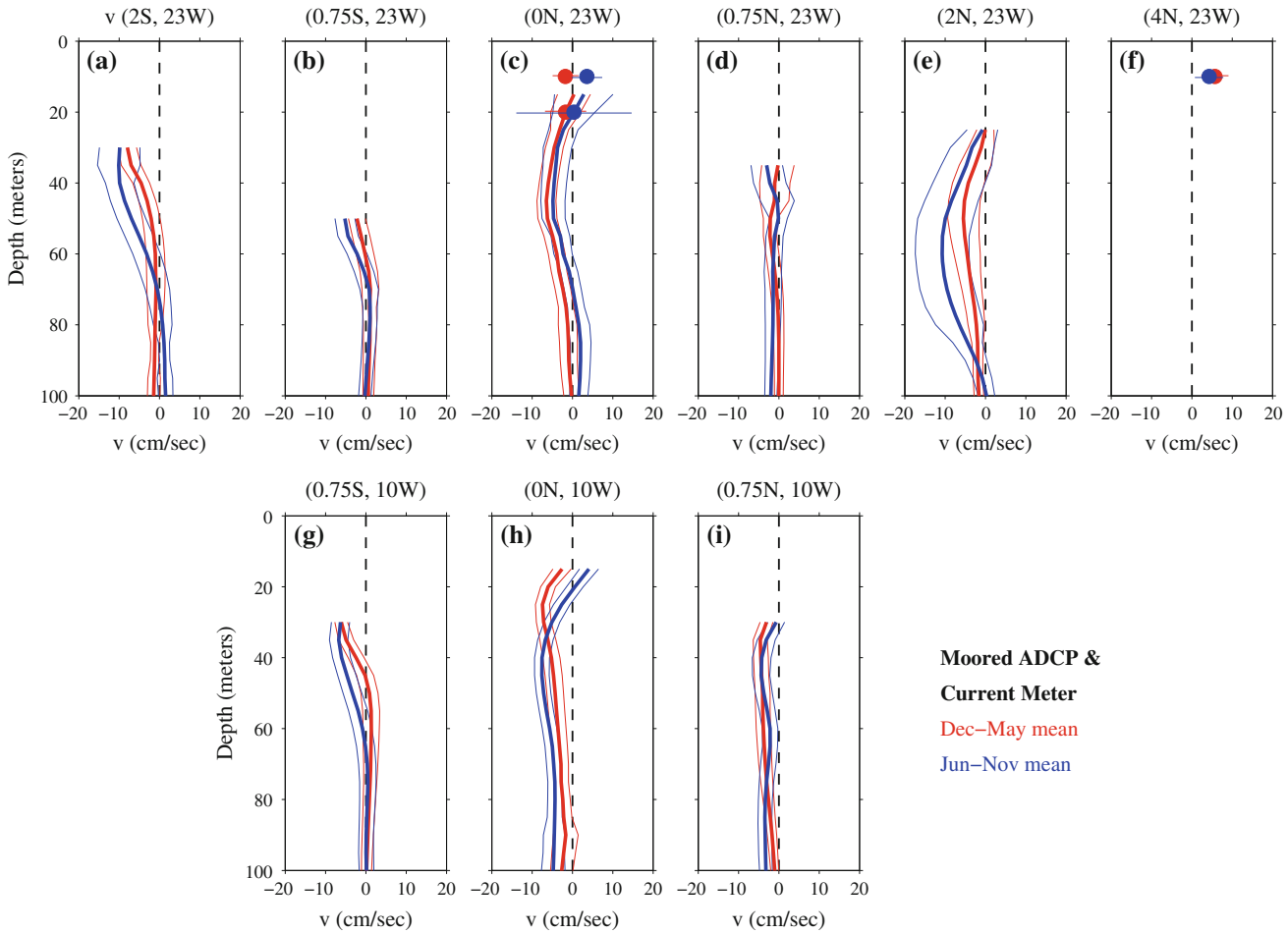

Fig. 14 Comparison of two-season mean meridional velocity derived from moored fixed-depth current meters (*circles*) and moored ADCPs (*thick lines*) at various latitudes along **a**–**f** 23°W and **g**–**i** 10°W. *Red* (*blue*) indicates mean during Dec–May (Jun–Nov). *Thin lines* denote the seasonal means ± total errors for the moored ADCP measurements, and the *circles with error bars* denote the seasonal means ± total errors for the fixed-depth current meter measurements

six-month mean meridional velocity from the moored ADCPs and fixed-depth current meters at the nine sites along 23°W and 10°W (Fig. 14) provides a measure of confidence in the GLORYS2V1 results (Fig. 15). First, the flow in the subsurface limb of the northern cell indeed appears to be stronger during Jun–Nov (compare thick blue and red lines in Figs. 14e, 15e)—unfortunately, there are no moored ADCP data available at 4°N, 23°W where the simulated seasonal difference at the nine sites studied here is largest (compare thick blue and red lines in Fig. 15f). Second, the northern TC shifts further southward during Jun–Nov with the near-surface meridional velocity becoming more positive at the equator along both longitudes (Figs. 14c, h, 15c, h) as well as at 0.75°S and 0.75°N along 10°W (Figs. 14g, i, 15g, i). However, due to the large uncertainties associated with the observed 6-month mean meridional velocities at most of these sites (Fig. 14), only the observed seasonal differences at 0°, 10°W (Fig. 14h) may be significant.

4 Summary and discussion

The tropical Atlantic has garnered significant scientific interest over the past two decades as coupled intraseasonal-to-multidecadal ocean–atmosphere variability in this region has been recognized to strongly influence fluctuations of the ITCZ complex, regional rainfall over bordering continents, as well as hurricane activity in the United States and Caribbean islands (e.g., Goldenberg et al. 2001; Okumura and Xie 2004; Sutton and Hodson 2005; Chang et al. 2006; Kushnir et al. 2006; Brandt et al. 2011b; Tokinaga and Xie 2011). Since the late 1990s, several major field programs have been initiated to monitor the circulation, hydrography, and air-sea fluxes in the central and eastern equatorial Atlantic with moored arrays and cross-equatorial cruises. In this study, shipboard and lowered ADCP velocity measurements collected by these programs were averaged and combined with estimates of the mean near-surface meridional velocity derived from

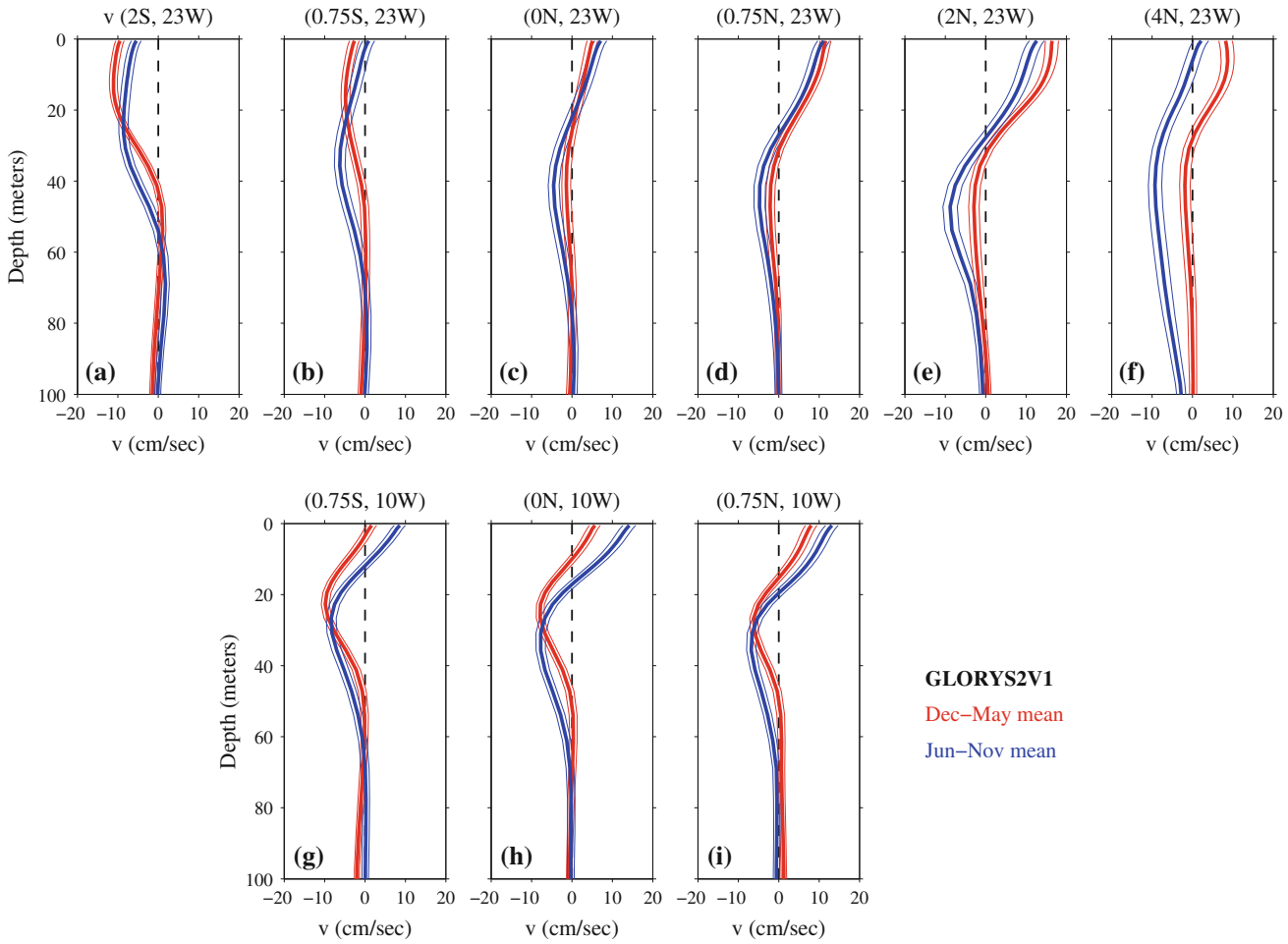

Fig. 15 Same as Fig. 14, except for GLORYS2V1 seasonal mean meridional velocities. *Thin lines* denote the seasonal means ± standard errors (assuming a decorrelation time scale of 10 days) for the GLORYS2V1 meridional velocities

drifters and Argo float surface drifts to describe for the first time the mean cross-equatorial and vertical structure of the meridional currents along 23°W and 10°W, and to provide a new tool with which to assess the realism of the tropical Atlantic circulation in OGCMs, assimilation models, and coupled climate models. Data from moored ADCPs and fixed-depth current meters in the region, the satellite-derived OSCAR product, and the global ocean reanalysis GLORYS2V1 were additionally used to evaluate the mean meridional velocity estimated from the combined ADCP and drifter-Argo data (ADCP+D) along 23°W and 10°W.

Analysis of the ADCP+D long-term mean structure of meridional velocity confirmed that the dominant circulation features along these longitudes in the upper 100 m of the water column are the TCs, with near-surface poleward flow and subsurface equatorward flow that is stronger in the northern cell than it is in the southern cell. The thickness of the surface limb of the TCs decreases between 23°W and 10°W consistent with the eastward shoaling of the thermocline or pycnocline (e.g., Philander and Pacanowksi 1986). Moreover, the northern cell was observed to shift further south of the equator consistent with the more southerly orientation of the winds along 10°W noted in Sect. 3.3, and a southward shift in maximum equatorial divergence and upwelling found in previous tropical Atlantic studies (e.g., Helber et al. 2007; Giordani and Caniaux 2011). Because of the deeper extent of the southern cell along both longitudes, the estimated mean meridional volume transport between 23°W and 10°W associated with the southern cell is stronger than that of the northern cell, that is −4.6 Sv compared with 2.3 Sv. The mean GLORYS2V1 meridional volume transport computed between 23°W and 10°W is very similar to the observed transport. Away from the continental boundaries, the magnitude of the GLORYS2V1 transport scales approximately by the longitudinal width, with the transport between 23°W and 10°W being nearly half of the transport between 35°W and 10°W and exhibiting a similar meridional structure (Fig. 6c, d). The basin-wide GLORYS2V1 meridional transport is comparable to previously reported

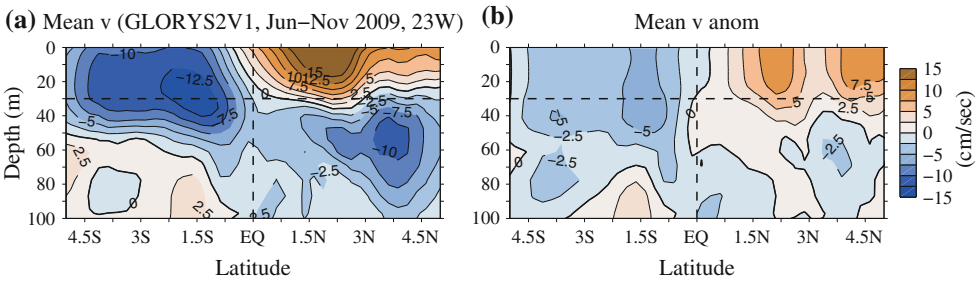

Fig. 16 Distribution of the **a** mean GLORYS2V1 meridional velocity along 23°W during Jun–Nov 2009 and **b** GLORYS2V1 meridional velocity anomaly during Jun–Nov 2009 relative to the two-season Jun–Nov mean shown in Fig. 10d. Contour interval is 2.5 cm s^{-1}

model estimates which typically range from 10 to 15 Sv (e.g., Hazeleger et al. 2003; Lohmann and Latif 2007), and is strongly influenced by western boundary currents such as the North Brazil Current and Undercurrent and therefore does not scale by the longitudinal width of the integration (Fig. 6c).

The structure of the TCs derived from the observations was sensitive to whether the mean ship-based ADCP meridional velocity was linearly extrapolated from 30 m depth up to the surface using mean drifter-Argo or OSCAR meridional velocity, or ADCP-derived estimates of the mean vertical shear between 30 and 40 m, with the best representation of the mean near-surface meridional currents resulting from vertical extrapolation to the mean drifter-Argo meridional velocity. However, based on comparisons with mean meridional velocities obtained from moored ADCPs and fixed-depth current meters, as well as GLORYS2V1, it is clear that more direct velocity measurements are needed near the maxima of poleward velocity in the surface limb of the TCs (typically between ±1° and ±4° of latitude) to better resolve the meridional flow and vertical current shear in the upper 30 m.

Combined analysis of the two-season means estimated from the ship-based ADCP, drifter-Argo, and moored velocity data, as well as from GLORYS2V1 indicated that the maximum poleward velocity in the surface limb of the TCs intensifies during December to May along 23°W when the cold tongue is typically absent or weak, whereas the maximum equatorward flow in the subsurface limb of the northern cell intensifies during June to November along both 23°W and 10°W when the cold tongue is most pronounced in boreal summer. These seasonal differences appear to be largely due to compensation between the seasonal variations of the geostrophic and ageostrophic (wind-driven) components of meridional velocity in the surface limb of the TCs, and the seasonality of geostrophic meridional velocity in the subsurface limb of the TCs. However, more long-term direct current measurements are needed in the upper 100 m to examine the robustness of this result (i.e., reducing uncertainties due to the relatively small sample sizes), in particular between ±1° and ±4° of latitude where the mean meridional velocities associated with the mean locations of the TCs, as well as the velocity fluctuations due to TIWs, are both strongest.

During boreal summer, subsurface meridional currents in the central and eastern equatorial Atlantic can advect interannual wind-driven warm temperature anomalies induced immediately north of the equator southward and possibly trigger non-canonical Atlantic Niño events (Richter et al. 2013; Lübbecke 2013), and similarly advect corresponding cold anomalies southward and possibly trigger anomalous cooling events such as in May–July 2009 (Foltz et al. 2012; Brandt et al. 2013). Concurrent with the May–July 2009 cooling event, the poleward flow in the surface limb of the TCs and southward flow in the subsurface limb of the northern TC both intensified in GLORYS2V1 relative to the two-season mean, and the northward flow in the subsurface limb of the southern TC weakened (Fig. 16). Thus, cold temperature anomalies induced near the equator were advected southward by interannually modified TCs. Unfortunately, there were insufficient in situ measurements to corroborate this finding with observations. With improved long-term measurements of meridional velocity in the tropical Atlantic, we will be able to examine more generally how the TCs themselves vary under such interannual wind forcing, and whether subsurface temperature anomalies generated during extreme events are advected by the seasonally strong or interannually intensified TCs.

Acknowledgments This research was carried out in part under the auspices of the Cooperative Institute for Marine and Atmospheric Studies (CIMAS), a Cooperative Institute of the University of Miami and the National Oceanic and Atmospheric Administration (NOAA), cooperative agreement # NA10OAR4320143. Additional support was provided by NOAA's Climate Program Office, NOAA's Atlantic Oceanographic and Meteorological Laboratory, the Global Drifter Program NOAA NA10OAR4320156, the Deutsche Bundesministerium für Bildung und Forschung, project RACE (03F0651B), and the Deutsche Forschungsgemeinschaft through SFB754. The authors thank the PIRATA program which makes PIRATA mooring and shipboard data sets freely available to the scientific community. The authors also thank Adam Houk, Andreas Funk, and Arne Körtzinger for help obtaining and processing additional moored and shipboard data sets. Output from the GLORYS2V1 reanalysis product was obtained through a collaborative agreement with Mercator Océan. The GLORYS reanalysis project received support from INSU-CNRS, Mercator Océan, Groupe Mission Mercator Coriolis and the European Community's Seventh Framework Programme FP7/2007–2013 under

grant agreement n°218812 (MyOcean). Nicolas Ferry and Laurent Parent are thanked for their helpful comments concerning GLORYS2V1 output. This study used velocities derived from Argo float surface trajectories of the YoMaHa'07 data set (Lebedev et al. 2007) which are provided by APDRC/IPRC. The OSCAR data were obtained from JPL Physical Oceanography DAAC and developed by Earth and Space Research. NCEP Reanalysis data are provided by the NOAA-CIRES Climate Diagnostics Center, Boulder, Colorado, USA, at their web site http://www.cdc.noaa.gov/. Comments from Gregory Foltz, Silvia Garzoli, Christopher Meinen, Paul Freitag, and two anonymous reviewers led to significant improvements in the manuscript.

References

Athié G, Marin F (2008) Cross-equatorial structure and temporal modulation of intraseasonal variability at the surface of the tropical Atlantic Ocean. J Geophys Res 113:C08020. doi:10.1029/2007JC004332

Athié G, Marin F, Treguier A-M, Bourlès B, Guiavarc'h C (2009) Sensitivity of near-surface tropical instability waves to submonthly wind forcing in the tropical Atlantic. Ocean Model 30:241–255. doi:10.1016/j.ocemod.2009.06.016

Barnier B, Madec G, Penduff T, Molines J-M, Treguier A-M, Le Sommer J, Beckmann A, Biastoch A, Böning C, Dengg J, Derval C, Durand E, Gulev S, Remy E, Talandier C, Theetten S, Maltrud M, McClean J, De Cuevas B (2006) Impact of partial steps and momentum advection schemes in a global ocean circulation model at eddy-permitting resolution. Ocean Dyn 56:543–567. doi:10.1007/s10236-006-0082-1

Benkiran M, Greiner E (2008) Impact of the incremental analysis updates on a real-time system of the North Atlantic Ocean. J Atmos Ocean Technol 25:2055–2073

Bloom SC, Takas LL, Da Silva AM, Ledvina D (1996) Data assimilation using incremental analysis updates. Mon Weather Rev 124:1256–1271

Bonjean F, Lagerloef GSE (2002) Diagnostic model and analysis of the surface currents in the tropical Pacific Ocean. J Phys Oceanogr 32:2938–2954

Bourlès B, Lumpkin R, McPhaden MJ, Hernandez F, Nobre P, Campos E, Yu L, Planton S, Busalacchi A, Moura AD, Servain J, Trotte J (2008) The PIRATA program: history, accomplishments, and future directions. Bull Am Meteorol Soc 89:1111–1125. doi:10.1175/2008BAMS2462.1

Brandt P, Schott FA, Provost C, Kartavtseff A, Hormann V, Bourlès B, Fischer J (2006) Circulation in the central equatorial Atlantic: mean and intraseasonal to seasonal variability. Geophys Res Lett 33:L07609. doi:10.1029/2005GL025498

Brandt P, Hormann V, Bourlès B, Fischer J, Schott FA, Stramma L, Dengler M (2008) Oxygen tongues and zonal currents in the equatorial Atlantic. J Geophys Res 113:C04012. doi:10.1029/2007JC004435

Brandt P, Hormann V, Körtzinger A, Visbeck M, Krahmann G, Stramma L, Lumpkin R, Schmid C (2010) Changes in the ventilation of the oxygen minimum zone of the tropical North Atlantic. J Phys Oceanogr 40:1784–1801. doi:10.1175/2010JPO4301.1

Brandt P, Caniaux G, Bourlès B, Lazar A, Dengler M, Funk A, Hormann V, Giordani H, Marin F (2011a) Equatorial upper-ocean dynamics and their interaction with the West African monsoon. Atmos Sci Lett 12:24–30. doi:10.1002/asl.287

Brandt P, Funk A, Hormann V, Dengler M, Greatbatch RJ, Toole JM (2011b) Interannual atmospheric variability forced by the deep equatorial Atlantic Ocean. Nature 43:497–500. doi:10.1038/nature10013

Brandt P, Funk A, Tantet A, Johns W, Fischer J (2013) The Equatorial Undercurrent in the central Atlantic and its relation to tropical Atlantic variability. Clim Dyn, submitted

Bunge L, Provost C, Kartavtseff A (2007) Variability in horizontal current velocities in the central and eastern equatorial Atlantic in 2002. J Geophys Res 112:C02014. doi:10.1029/2006JC003704

Chang P, Yamagata T, Schopf P, Behera SK, Carton J, Kessler WS, Meyers G, Qu T, Schott F, Shetye S, Xie SP (2006) Climate fluctuations of tropical coupled systems—the role of ocean dynamics. J Clim 19:5122–5174. doi:10.1175/JCLI3903.1

Da-Allada CY, Alory G, du Penhoat Y, Kestenare E, Durand F, Hounkonnou NM (2013) Seasonal mixed-layer salinity balance in the tropical Atlantic Ocean: mean state and seasonal cycle. J Geophys Res 118:332–345. doi:10.1029/2012JC008357

Düing W, Hisard P, Katz E, Meincke J, Miller L, Moroshkin KV, Philander G, Ribnikov AA, Voigt K, Weisberg R (1975) Meanders and long waves in the equatorial Atlantic. Nature 257:280–284. doi:10.1038/257280a0

Dutrieux P, Menkes CE, Vialard J, Flament P, Blanke B (2008) Lagrangian study of tropical instability vortices in the Atlantic. J Phys Oceanogr 38:400–417. doi:10.1175/2007JPO3763.1

Ferry N, Parent L, Garric G, Barnier B, Jourdain NC, MERCATOR Group (2010) Mercator global Eddy permitting ocean reanalysis GLORYS1V1: description and results. Mercator Ocean Q Newsl 36:15–27

Fischer J, Brandt P, Dengler M, Müller M, Symonds D (2003) Surveying the upper ocean with the Ocean Surveyor: a new phased array Doppler current profiler. J Atmos Ocean Technol 20:742–751

Foltz GR, Carton JA, Chassignet EP (2004) Tropical instability vortices in the Atlantic Ocean. J Geophys Res 109:C03029. doi:10.1029/2003JC001942

Foltz GR, McPhaden MJ, Lumpkin R (2012) A strong Atlantic meridional mode event in 2009: the role of mixed layer dynamics. J Clim 25:363–380. doi:10.1175/JCLI-D-11-00150.1

Freitag HP, McPhaden MJ, Meinig C, Plimpton P (2003) Mooring motion bias of point Doppler current meter measurements. In: Proceedings of the IEEE seventh working conference on current measurement technology, San Diego, CA, 13–15 Mar 2003, IEEE, Piscataway, NJ, pp 155–160

Garzoli SL (1987) Forced oscillations on the equatorial Atlantic Basin during the seasonal response of the Equatorial Atlantic Program (1983–1984). J Geophys Res 5089(C5):5089–5100. doi:10.1029/JC092iC05p05089

Giordani H, Caniaux G (2011) Diagnosing vertical motion in the equatorial Atlantic. Ocean Dyn 61:1995–2018. doi:10.1007/s10236-011-0467-7

Goldenberg SB, Landsea C, Mestas-Nunez AM, Gray WM (2001) The recent increase in Atlantic hurricane activity. Science 293:474–479

Grodsky SA, Carton JA, Provost C, Servain J, Lorenzzetti JA, McPhaden MJ (2005) Tropical instability waves at 0 N, 23 W in the Atlantic: a case study using Pilot Research Moored Array in the Tropical Atlantic (PIRATA) mooring data. J Geophys Res 110:C08010. doi:10.1029/2005JC002941

Hazeleger W, de Vries P, Friocourt Y (2003) Sources of the Equatorial Undercurrent in the Atlantic in a high-resolution ocean model. J Phys Oceanogr 33:677–693

Helber RW, Weisberg RH, Bonjean F, Johnson ES, Lagerloef GSE (2007) Satellite-derived surface current divergence in relation to tropical Atlantic SST and wind. J Phys Oceanogr 33:1357–1375

Hormann V, Brandt P (2007) Atlantic Equatorial Undercurrent and associated cold tongue variability. J Geophys Res 112:C06017. doi:10.1029/2006JC003931

Hormann V, Brandt P (2009) Upper equatorial Atlantic variability during 2002 and 2005 associated with equatorial Kelvin waves. J Geophys Res 114:C03007. doi:10.1029/2008JC005101

Hormann V, Lumpkin R, Perez RC (2013) A generalized method for estimating the structure of the equatorial Atlantic cold tongue: application to drifter observations. J Atmos Ocean Technol 30:1884–1895. doi:10.1175/JTECH-D-12-00173.1

Hummels R, Dengler M, Bourlès B (2013) Seasonal and regional variability of upper ocean diapycnal heat flux in the Atlantic cold tongue. Prog Oceanogr 111:52–74. doi:10.1016/j.pocean.2012.11.001

Johnson G, McPhaden MJ, Firing E (2001) Equatorial Pacific Ocean horizontal velocity, divergence, and upwelling. J Phys Oceanogr 31:839–849

Johnson G, Sloyan BM, Kessler WS, McTaggart KE (2002) Direct measurements of upper ocean currents and water properties across the tropical Pacific Ocean during the 1990s. Prog Oceanogr 52:31–61

Jouanno J, Marin F, du Penhoat Y, Molines J-M (2013) Intraseasonal modulation of the surface cooling in the Gulf of Guinea. J Phys Oceanogr 43:382–401. doi:10.1175/JPO-D-12-053.1

Kolodziejczyk N, Bourlès B, Marin F, Grelet J, Chuchla R (2009) Seasonal variability of the Equatorial Undercurrent at 10 W as inferred from recent in situ observations. J Geophys Res 114:C06014. doi:10.1029/2008JC004976

Kushnir Y, Robinson WA, Chang P, Robertson AW (2006) The physical basis for predicting Atlantic sector seasonal-to-interannual climate variability. J Clim 19:5949–5970

Lebedev KV, Yoshinari H, Maximenko NA, Hacker PW (2007) Velocity data assessed from trajectories of Argo floats at parking level and at the sea surface. IPRC Technical Note, No. 4(2), 12 June 2007, p 16

Legeckis R (1977) Long waves in the eastern equatorial Pacific Ocean: a view from a geostationary satellite. Science 197:1179–1181

Legeckis R, Reverdin G (1987) Long waves in the equatorial Atlantic Ocean during 1983. J Geophys Res 92:2835–2842

Liu Z, Philander SGH, Pacanowski RC (1994) A GCM study of tropical–subtropical upper-ocean water exchange. J Phys Oceanogr 24:2606–2623

Lohmann K, Latif M (2007) Influence of El Niño on the upper-ocean circulation in the tropical Atlantic Ocean. J Clim 20:5012–5018. doi:10.1175/JCLI4292.1

Lübbecke JF (2013) Tropical Atlantic warm events. Nat Geosci 6:22–23. doi:10.1038/ngeo1685

Lumpkin R, Garraffo Z (2005) Evaluating the decomposition of tropical Atlantic drifter observations. J Atmos Ocean Technol 22:1403–1415

Lumpkin R, Garzoli SL (2005) Near-surface circulation in the tropical Atlantic Ocean. Deep Sea Res I 52:495–518. doi:10.1016/j.dsr.2004.09.001

Lumpkin R, Grodsky S, Rio M-H, Centurioni L, Carton J, Lee D (2013) Removing spurious low-frequency variability in surface drifter velocities. J Atmos Ocean Technol 30(2):353–360. doi:10.1175/JTECH-D-12-00139.1

Madec G (2008) NEMO ocean engine. Note du pole de modélisation, Institut Pierre-Simon Laplace (IPSL), France, No 27, ISSN No 1288-1619, p 201

Malanotte-Rizzoli P, Hedstrom K, Arango H, Haidvogel DB (2000) Water mass pathways between the subtropical and tropical ocean in a climatological simulation of the North Atlantic ocean circulation. Dyn Atmos Ocean 32:331–371

McCreary JP, Lu P (1994) Interaction between the subtropical and equatorial ocean circulations: the subtropical cell. J Phys Oceanogr 24:466–497

Menkes CE, Flament P, Dandonneau Y, Masson S, Biessy B, Marchal E, Eldin G, Grelet J, Montel Y, Morlière A, Lebourges-Dhaussy A, Moulin C, Champalbert G, Herbland A (2002) A whirling ecosystem in the equatorial Atlantic. Geophys Res Lett 29:1553. doi:10.1029/2001GL014576

Molinari RL, Bauer S, Snowden D, Johnson GC, Bourlès B, Gouriou Y, Mercier H (2003) A comparison of kinematic evidence for tropical cells in the Atlantic and Pacific oceans. In: Goni GJ, Malanotte-Rizzoli P (eds) IAPSO special issue: interhemispheric water exchange in the Atlantic Ocean, Elsevier Oceanography Series 68:269–286

Niiler PP, Paduan JD (1995) Wind-driven motions in the northeast Pacific as measured by Lagrangian drifters. J Phys Oceanogr 25:2819–2830

Okumura Y, Xie S-P (2004) Interaction of the Atlantic equatorial cold tongue and the African monsoon. J Clim 17:3589–3602

Pazan SE, Niiler PP (2001) Recovery of near-surface velocity from undrogued drifters. J Atmos Ocean Technol 18:476–489

Perez RC, Kessler WS (2009) The three-dimensional structure of tropical cells in the central equatorial Pacific Ocean. J Phys Oceanogr 39:27–49. doi:10.1175/2008JPO4029.1

Perez RC, Cronin MF, Kessler WS (2010) Tropical cells and a secondary circulation near the northern front of the equatorial Pacific cold tongue. J Phys Oceanogr 40:2091–2106. doi:10.1175/2010JPO4366.1

Perez RC, Lumpkin R, Johns WE, Foltz GR, Hormann V (2012) Interannual variations of Atlantic tropical instability waves. J Geophys Res 117:C03011. doi:10.1029/2011JC007584

Pham DT, Verron J, Roubaud M-C (1998) A singular evolutive extended Kalman filter for data assimilation in oceanography. J Mar Syst 16:323–340

Philander SGH, Pacanowksi RC (1986) A model of the seasonal cycle in the tropical Atlantic Ocean. J Geophys Res 91(C12):14192–14206

Plimpton PE, Freitag HP, McPhaden MJ (2004) Processing of subsurface ADCP data in the equatorial Pacific. NOAA Tech. Memo OAR PMEL-125, NOAA/Pacific Marine Environmental Laboratory, Seattle, WA, p 41

Provost C, Arnault S, Chouaib N, Kartavtseff A, Bunge L, Sultan E (2004) TOPEX/Poseidon and Jason equatorial sea surface slope anomaly in the Atlantic in 2002: comparison with wind and current measurements at 23 W. Mar Geod 27:31–45

Qiao L, Weisberg RH (1995) Tropical instability wave kinematics: observations from the Tropical Instability Wave Experiment (TIWE). J Phys Oceanogr 100:8677–8693

Rabe B, Schott FA, Köhl A (2008) Mean circulation and variability of the tropical Atlantic during 1952–2001 in the GECCO assimilation fields. J Phys Oceanogr 38:177–192

Richter I, Behera SK, Masumoto Y, Taguchi B, Sasaki H, Yamagata T (2013) Multiple causes of interannual sea surface temperature variability in the equatorial Atlantic Ocean. Nat Geosci 6:43–47. doi:10138/ngeo1660

Schott FA, Dengler M, Brandt P, Affler K, Fischer J, Bourlès B, Gouriou Y, Molinari RL, Rhein M (2003) The zonal currents and transports at 35 W in the tropical Atlantic. Geophys Res Lett 30(7):1349. doi:10.1029/2002GL016849

Schott F, McCreary J, Johnson G (2004) Shallow overturning circulations of the tropical-subtropical oceans. In: Wang C, Xie S-P, Carton JA (eds) Earth climate: the ocean–atmosphere interaction, AGU Geophysical Monograph Series 147:261–304

Seo H, Xie S-P (2011) Response and impact of equatorial ocean dynamics and tropical instability waves in the tropical Atlantic under global warming: a regional coupled downscaling study. J Geophys Res 116:C03026. doi:10.1029/2010JC006670

Seo H, Jochum M, Murtugudde R, Miller AJ, Roads JO (2007) Feedback of tropical instability-wave-induced atmospheric variability onto the ocean. J Clim 20:5842–5855. doi:10.1175/2007JCLI1700.1

Simmons A, Uppala S, Dee D, Kobayashi S (2007) ERAInterim: new ECMWF reanalysis products from 1989 onwards. ECMWF Newsl 110:25–35

Steger JM, Carton JA (1991) Long waves and eddies in the tropical Atlantic Ocean: 1984–1990. J Geophys Res 96:15161–15171

Subramaniam A, Mahaffey C, Johns W, Mahowald N (2013) Equatorial upwelling enhances nitrogen fixation in the Atlantic Ocean. Geophys Res Lett 40:1766–1771. doi:10.1002/grl.50250

Sutton RT, Hodson DLR (2005) Atlantic Ocean forcing of North American and European summer climate. Science 309:115–118. doi:10.1175/JCLI4038.1

Tokinaga H, Xie S-P (2011) Weakening of the equatorial Atlantic cold tongue over the past six decades. Nature Geosci 4:222–226. doi:10.1038/ngeo1078

Tranchant B, Testut C-E, Renault L, Ferry N, Birol F, Brasseur P (2008) Expected impact of the future SMOS and Aquarius Ocean surface salinity missions in the Mercator Ocean operational systems: new perspectives to monitor ocean circulation. Remote Sens Environ 112:1476–1487

Visbeck M (2002) Deep velocity profiling using lowered acoustic Doppler current profilers: bottomtrack and inverse solutions. J Atmos Ocean Technol 19:794–807

von Schuckmann K, Brandt P, Eden C (2008) Generation of tropical instability waves in the Atlantic Ocean. J Geophys Res 113:C08034. doi:10.1029/2007JC004712

Weisberg RH, Weingartner TJ (1988) Instability waves in the equatorial Atlantic Ocean. J Phys Oceanogr 18:1641–1657